Acta Materialia 195 (2020) 597–610

Contents lists available at ScienceDirect

Acta Materialia

journal homepage: www.elsevier.com/locate/actamat

Full length article

Interactions between ⟨a⟩ dislocations and three-dimensional $\{11\bar{2}2\}$ twin in Ti

Mingyu Gong[a,b], Shun Xu[a], Laurent Capolungo[c], Carlos N Tomé[c], Jian Wang[a,b,*]

[a] Mechanical and Materials Engineering, University of Nebraska-Lincoln, Lincoln, NE 68588, USA
[b] Nebraska Center for Materials and Nanoscience, University of Nebraska-Lincoln, Lincoln, NE 68588, USA
[c] MST-8, Los Alamos National Laboratory, Los Alamos, NM 87544, USA

ARTICLE INFO

Article History:
Received 30 March 2020
Revised 4 May 2020
Accepted 18 May 2020
Available online 3 June 2020

Keywords:
Dislocation
Twin
Slip transmission
Secondary twinning
Molecular dynamics

ABSTRACT

⟨**a**⟩dislocations on basal or prismatic planes and $\{11\bar{2}2\}$ compression twins are commonly activated in deformed Titanium (Ti). In the present work, their interactions are investigated by both crystallographic analysis and atomistic simulations. For a three-dimensional $\{11\bar{2}2\}$ twin, we firstly analyze seven possible twin boundaries (TBs) bonding two low index planes in matrix and twin. Next, we focus on the two lower energy boundaries, $\{11\bar{2}2\}_{M/T} \parallel \{11\bar{2}2\}_{T/M}$ coherent twin boundary (CTB) and $\{\bar{1}2\bar{1}1\}_{M/T} \parallel \{\bar{1}2\bar{1}\bar{1}\}_{T/M}$. Depending on dislocation character and boundary type, we define four types of interactions between ⟨**a**⟩ dislocations and these TBs. Further, we predict possible dislocation reactions on/across TBs using crystallographic analysis according to the deformation compatibility and the change in elastic energy, such as twinning/detwinning of the primary twin, slip transmission and secondary twinning, for each type of interaction. Molecular dynamics (MD) simulations are then conducted for all interactions under pre-selected loadings in order to explore the dynamic process associated with each of these interactions and examine the predicted reactions. MD simulations predict that the interaction between ⟨**a**⟩ dislocations and some facets can lead to the formation of secondary twins and ⟨**a**⟩ dislocations on basal or prismatic planes in twins, and reveal the possibility of forming ⟨**c**⟩ and ⟨**c** + **a**⟩ dislocations in twins. Moreover, some of the possible reactions take place on lateral TBs other than CTBs.

1. Introduction

Titanium and its alloys have wide applications in the aerospace, chemical and medical implants industries because of their specific strength, excellent corrosion resistance and good biocompatibility [1–3]. A fundamental understanding of the deformation mechanisms activated during plasticity is essential for the development of constitutive laws of Ti alloys that can be used to predict the deformation behavior and optimize the forming routes of Ti alloys [4–8]. α-Ti with the hexagonal close packed (HCP) crystal structure at room temperature deforms plastically via dislocation slip and twinning. These dislocations are associated with prismatic ⟨**a**⟩ slip, basal ⟨**a**⟩ slip and pyramidal ⟨**c** + **a**⟩ slip. Prismatic ⟨**a**⟩ and basal ⟨**a**⟩ slip are more easily activated due to their lower critical resolved shear stress (CRSS) compared with pyramidal ⟨**c** + **a**⟩ slip [9–12]. However, ⟨**a**⟩ dislocations cannot contribute to plasticity along the ⟨**c**⟩ axis. Thus, twinning occurs in competition with ⟨**c** + **a**⟩ slip to accommodate plastic deformation along ⟨**c**⟩ axis. $\{\bar{1}012\}$ tension twins and $\{11\bar{2}2\}$ compression twins are commonly activated at room temperature [13–15].

⟨**a**⟩ dislocations and twins are activated concurrently during mechanical deformation. Therefore, interactions between dislocations [16–20], twins [21–27] and dislocation and twin [25, 28–31] will inevitably take place. Regarding latent hardening induced by dislocation-dislocation interactions, experimental measurements indicate that the effective slip resistance scales as the square root of dislocation density [16–18], and the effective interaction strength between two slip systems is often expressed by means of a generalized Taylor-like equation as proposed by Zaoui et al. [32]. Twin-twin interactions can cause work hardening [33–36] and have been shown to initiate cracks [35, 37–40]. As an incoming twin is obstructed by a pre-existing twin [21, 41, 42], twin-twin junctions (TTJs) and associated boundaries (TTBs) form [42–44]. These subsequently affect twinning, detwinning, and slip processes [43, 45, 46]. When dislocations approach a twin, it may interact with twin boundaries (TBs). The interactions between TBs and dislocations induce dislocation reactions at the interface [47–53], twinning/detwinning of the primary twin [54–58], and secondary twinning in pre-existing twins [28, 59]. Consequently, different interactions result in complex mechanical response. For example, Capolungo et al. [60] performed

* Corresponding author at: Mechanical and Materials Engineering, University of Nebraska-Lincoln, Lincoln, NE 68588, USA.
E-mail address: wangj6@gmail.com (J. Wang).

https://doi.org/10.1016/j.actamat.2020.05.046

sets of temperature jump tests in Zr and showed that the interactions between dislocations and $\{\bar{1}012\}$ twins induced less hardening than the interactions between dislocations and $\{11\bar{2}2\}$ twins. The associated mechanisms need further investigation.

The interactions between $\langle \mathbf{a} \rangle$ dislocations and $\{\bar{1}012\}$ twins have been investigated extensively using geometrical models (GMs) [61–66], experimental characterizations [6, 47–51, 67–75] and atomistic simulations [52–58, 76, 77]. GMs predict the: (i) complete transmission of a screw $\langle \mathbf{a} \rangle$ dislocation into the twin whereby the transmitted dislocation remains unaltered [52, 53, 64, 66], (ii) the transmission of two mixed $\langle \mathbf{a} \rangle$ dislocations with the same screw component into the twin as a $\langle \mathbf{c}+\mathbf{a} \rangle$ dislocation [53, 64, 66], and (iii) the transmission of two mixed $\langle \mathbf{a} \rangle$ dislocations with the opposite screw component into a $\langle \mathbf{c} \rangle$ dislocation in twins [72]. Molodov et al. [47] utilized optical microscopy to observe slip traces in matrix and twin, and confirmed that the transmission of screw $\langle \mathbf{a} \rangle$ dislocations is consistent with GM's prediction. Moreover, $\langle \mathbf{c}+\mathbf{a} \rangle$ dislocations have been characterized in the vicinity of TBs and within twins in Mg [48, 49] and Zn [50, 51] by transmission electron microscopy (TEM). Wang et al. [78] performed *in-situ* tension test in TEM and showed that dislocation slip induce twin growth. Further, atomistic simulations predicted similar twin growth during dislocation-twin interactions. The majority of atomistic simulations are conducted in a two-dimensional (2D) framework, and reveal that screw $\langle \mathbf{a} \rangle$ dislocations transmit into the same dislocation in twin [52] and mixed $\langle \mathbf{a} \rangle$ dislocations result in twinning/detwinning of the primary twins [54–58, 76, 77]. However, some of the experimental observations and predictions by GMs cannot be rationalized using a 2D framework. Gong et al. [53] first simulated the interaction between basal $\langle \mathbf{a} \rangle$ dislocations and a 3D $\{\bar{1}012\}$ twin for different dislocation character and twin boundaries. In addition to the findings reported in 2D simulations, they found that as two mixed $\langle \mathbf{a} \rangle$ dislocations react with the lateral side of a twin, they transmit into the twin as a $\langle \mathbf{c}+\mathbf{a} \rangle$ dislocation. They also noticed that the local stress field associated with the lateral side of a 3D twin facilitates cross-slip of screw $\langle \mathbf{a} \rangle$ dislocations, resulting in formation of jogs and basal stacking faults.

As for the interactions between $\langle \mathbf{a} \rangle$ dislocations and $\{11\bar{2}2\}$ twins, the Correspondence Matrix Rule (CMR, one of the GMs) [65, 79, 80] was used to analyze the crystallographic transformation of slip planes and slip vectors during the reorientation from matrix to $\{11\bar{2}2\}$ twin. Based on the CMR calculation, there is no slip system in the $\{11\bar{2}2\}$ twin corresponding to basal $\langle \mathbf{a} \rangle$ slip or prismatic $\langle \mathbf{a} \rangle$ slip in matrix. This does not fully agree with experimental observations. For example, only $\langle \mathbf{a} \rangle$ dislocations are characterized and reported in the matrix while $\langle \mathbf{a} \rangle$, $\langle \mathbf{c} \rangle$ and $\langle \mathbf{c}+\mathbf{a} \rangle$ dislocations have been shown to coexist in $\{11\bar{2}2\}$ twins [74, 81–83], mostly in the vicinity of TBs. This implies that the formation of $\langle \mathbf{c} \rangle$ and $\langle \mathbf{c}+\mathbf{a} \rangle$ dislocations in the twin is possibly resulted from the interactions between $\langle \mathbf{a} \rangle$ dislocations in matrix and the twin. This discrepancy between CMR analysis and experiments may originate from the fact that the character of the interaction boundary is not taken into account. Moreover, possible generation of secondary twinning is not considered in CMR. In Ti, $\{11\bar{2}2\} \rightarrow \{\bar{1}012\}$ and $\{11\bar{2}2\} \rightarrow \{11\bar{2}1\}$ double twins are often observed [28, 84]. Xu et al. [28, 29] proposed that $\{10\bar{1}2\}$ secondary twins nucleate by dissociation of prismatic $\langle \mathbf{a} \rangle$ dislocations on TBs and $\{11\bar{2}1\}$ secondary twins nucleate by dissociation of basal $\langle \mathbf{a} \rangle$ dislocations on TBs. Serra et al. [56] conducted MD simulations with a 2D twin and found that an edge basal $\langle \mathbf{a} \rangle$ dislocation is blocked by the $\{11\bar{2}2\}$ CTB while a mixed basal $\langle \mathbf{a} \rangle$ dislocation with a mixed leading partial dislocation may transmit into the twin. There is no report on simulations of interactions between prismatic $\langle \mathbf{a} \rangle$ dislocations and $\{11\bar{2}2\}$ twins because of the difficulty in constructing a 2D simulation model with the right periodicity along both, the zone axis of the twin and the line of dislocations. In addition, current 2D MD simulations cannot explain the formation of $\langle \mathbf{c} \rangle$ and $\langle \mathbf{c}+\mathbf{a} \rangle$ dislocations within twins.

In this work, we systematically investigate interactions between prismatic $\langle \mathbf{a} \rangle$ and basal $\langle \mathbf{a} \rangle$ dislocations and a 3D $\{11\bar{2}2\}$ twin in Ti by using crystallographic analysis and MD simulations. Characteristic boundaries associated with 3D $\{11\bar{2}2\}$ twins are firstly identified based on the crystallography of a $\{11\bar{2}2\}$ twin and interface energies. As for crystallographic analysis of dislocation-twin interactions, we deal with the requirement of deformation compatibility by using Werner's geometric model [85] to predict possible reactions with respect to the type of TBs and the character of incoming dislocations. Furthermore, Frank's criteria [86] is employed to evaluate the change in the elastic energy of dislocations involved in the reactions. MD simulations are then performed to explore the dynamic process of possible reactions. Our results reveal that the combined application of crystallographic analysis, Frank's criteria and 3D MD simulations for dislocation-twin interactions are needed in order to provide a comprehensive and more realistic understanding of dislocation-twin interactions.

2. Characteristic twin boundaries of three-dimensional $\{11\bar{2}2\}$ twin

Twins are 3D domains inside grains. The definition of normal-, forward- and lateral-TBs corresponds to twin propagation along twin normal $\mathbf{K_1}$, twinning shear $\boldsymbol{\eta_1}$ and zone axis $\boldsymbol{\lambda}$, respectively [87, 88]. Normal-TBs consist of the CTB and ledges on it associated with the pileup of twinning disconnections/dislocations (TDs). Forward- and lateral-TBs form as a result of pileup of TDs. The interaction of dislocations with a 3D twin is eventually determined by the reaction of the incoming dislocations with these TBs.

Fig. 1(a) and (b) shows the dichromatic complex associated with $\{11\bar{2}2\}$ twinning viewed along -$\boldsymbol{\lambda}$ and -$\boldsymbol{\eta_1}$ directions, corresponding to bright side (BS) and dark side (DS) views of a twin. The dichromatic

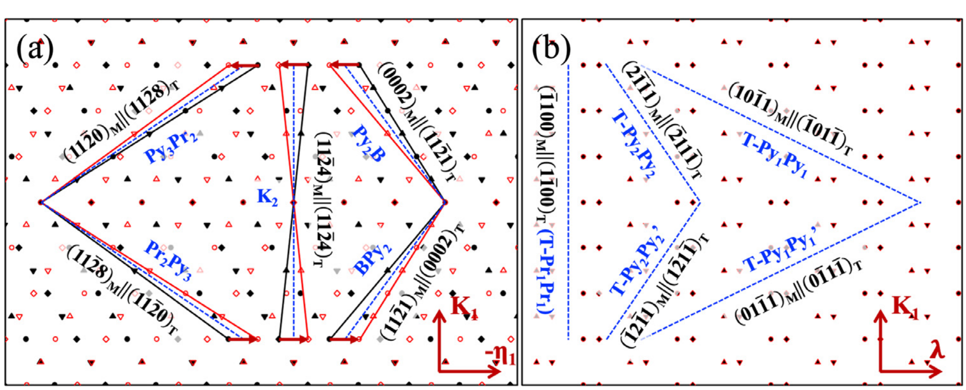

Fig. 1. Dichromatic complex associated with $\{11\bar{2}2\}$ twinning viewed along (a) -$\boldsymbol{\lambda}$ direction to predict forward-TBs and (b) -$\boldsymbol{\eta_1}$ direction to predict lateral-TBs. Red symbols represent atoms in twin and black symbols represent atoms in matrix. The circles, positive/inverted triangles, and diamonds represent atoms with different coordinates along the out of the paper.

Table 1
Possible interfaces associated with $\{11\bar{2}2\}$ twinning.

Interface	Twist/tilt angle	Type	Energy (mJ/m^2)
CTB	0°	Normal-TB	285
BPy_2/Py_2B	8.01° (Tilt)	Forward-TB	760
Pr_2Py_3/Py_3Pr_2	3.77° (Tilt)	Forward-TB	685
K_2	12.32° (Tilt)	Forward-TB	880
T-Pr_1Pr_1	12.32° (Twist)	Lateral-TB	400
T-Py_1Py_1/T-Py_1Py_1'	5.42° (Twist)	Lateral-TB	377
T-Py_2Py_2/T-Py_2Py_2'	10.17° (Twist)	Lateral-TB	265

complex in BS view (Fig. 1(a)) shows possible forward-TBs which are tilt boundaries with three types of possible interfaces, $\{0002\}_M \parallel \{11\bar{2}1\}_T$ or $\{11\bar{2}1\}_M \parallel \{0002\}_T$ (referred to as Py_2B or BPy_2), $\{11\bar{2}0\}_M \parallel \{11\bar{2}8\}_T$ or $\{11\bar{2}8\}_M \parallel \{11\bar{2}0\}_T$ (referred to as Py_3Pr_2 or Pr_2Py_3), and a conjugate TB $\{11\bar{2}4\}_M \parallel \{11\bar{2}4\}_T$ (referred to as K_2). For Ti with lattice constants a = 2.95 Å and c = 4.68 Å, BPy_2 or Py_2B step can be described as coherency disclination with a rotation angle of 8.01° as recently proposed by Gong et al. [87] and Hirth et al. [89]. Similarly, Pr_2Py_3 or Py_3Pr_2 step has disclination character with a rotation angle of 3.77°, and K_2 step has disclination character with a rotation angle of 12.32°. Fig. 1(b) shows the dichromatic complex in DS view. The lateral-TBs could be three types of twist boundaries, $\{1\bar{1}00\}_M \parallel \{\bar{1}100\}_T$ (referred to as T-Pr_1Pr_1), $\{01\bar{1}1\}_M \parallel \{0\bar{1}1\bar{1}\}_T$ or $\{10\bar{1}1\}_M \parallel \{\bar{1}01\bar{1}\}_T$ (referred to as T-Py_1Py_1 or T-Py_1Py_1'), and a $\{\bar{1}2\bar{1}1\}_M \parallel \{1\bar{2}1\bar{1}\}_T$ or $\{2\bar{1}\bar{1}1\}_M \parallel \{\bar{2}11\bar{1}\}_T$ (referred to as T-Py_2Py_2 or T-Py_2Py_2'), with the corresponding twist angles of 12.32°, 5.42° and 10.17°, respectively.

The interface energy of these possible TBs with coherent structure are calculated (Table 1) using molecular statics simulations [90] with the embedded atom method (EAM) interatomic potential developed by Zope and Mishin [91]. The normal-TB CTB, and three lateral-TBs T-Pr_1Pr_1, T-Py_1Py_1/T-Py_1Py_1' and T-Py_2Py_2/T-Py_2Py_2' have low interface energy of 285 mJ/m^2, 400 mJ/m^2, 377 mJ/m^2 and 265 mJ/m^2, respectively.

We create a 3D twin with the two lowest energy boundaries CTB and T-Py_2Py_2, as shown in Fig. 2(a). Construction of the simulation model starts with a 40 × 40 × 40 nm single crystal cell with x-axis along $[\bar{1}\bar{1}23]_M$ direction, y-axis normal to $(11\bar{2}2)_M$ plane and z-axis along $[\bar{1}100]_M$ direction. A 3D $(11\bar{2}2)$ twin is created according to the shear-shuffle mechanism associated with $\{11\bar{2}2\}$ twinning [90]. With the application of the anisotropic Barnett-Lothe solutions [92] for the displacement field of a dislocation, TD dipoles which are infinitely long in x-direction are introduced into the model every three $(11\bar{2}2)_M$ planes. TDs with Burgers vector $\pm \frac{2a^2-c^2}{3(a^2+c^2)}[\bar{1}\bar{1}23]$ [90, 93, 94] pile up on $(\bar{1}2\bar{1}1)_M$ and $(2\bar{1}\bar{1}1)_M$ planes, forming twist walls. With further atomic shuffling, the 3D $(11\bar{2}2)$ twin shown in Fig. 2(a) is constructed. Observed along the x-direction, the twin structure has a hexagonal shape outlined by two types of boundaries, CTBs and T-Py_2Py_2/T-Py_2Py_2'. The created structure is then relaxed for 100 ps at 10 K with periodic boundary condition in x- and z-direction and fixed boundary condition in y-direction. Fig. 2(b) shows the relaxed twin having a near-cylindrical shape with 5 nm radius. We observed four characteristic boundaries, CTBs, T-Pr_1Pr_1, T-Py_1Py_1/T-Py_1Py_1', and T-Py_2Py_2/T-Py_2Py_2' that have low energy.

3. Crystallographic analysis of dislocation-twin interactions

Dislocation reactions taking place on/across characteristic TBs may result in slip transmission, twinning/detwinning of the primary twin and secondary twinning in the primary twin. Slip transmission means transferring of dislocations across TBs, achieving propagation of plastic deformation from matrix to twin microscopically. For convenience in describing twinning, PTDs and STDs refer to TDs associated with primary twinning and secondary twinning, respectively. Twinning/detwinning of the primary twin takes place via dissociation of the incoming lattice dislocations into PTDs. Secondary twinning enables propagation of plastic deformation from matrix to twin as well, while the deformation domain is accompanied by reorientation. Secondary twinning accomplished by glide of STDs can be treated as slip transmission to some extent in crystallographic analysis, in which the outgoing dislocations are STDs.

Three factors, geometric slip continuity, change in elastic energy and kinetic energy barrier associated with the reaction greatly affect the relative likelihood of all potential different reactions. Geometric slip continuity and the change in elastic energy can be considered in crystallographic analysis by applying Werner's GM [85] and Frank's criteria [86]. Although kinetic energy barrier associated with a reaction is not easily assessed by molecular statics simulations, likely or easily-happened reactions can be explored by using molecular dynamics simulation.

3.1. Crystallographic analysis

All possible reactions are related to slip plane and slip vector of the incoming and outgoing dislocations/TDs, character of twin boundaries, and stress condition. In our study, there are three Burgers vectors, $\langle \mathbf{a_1} \rangle = \left[2\bar{1}\bar{1}0\right]$, $\langle \mathbf{a_2} \rangle = \left[\bar{1}2\bar{1}0\right]$, and $\langle \mathbf{a_3} \rangle = \left[\bar{1}\bar{1}20\right]$, for incoming $\langle \mathbf{a} \rangle$ dislocations that glide on (0001) or $\{1\bar{1}00\}$ slip planes. To generalize possible reactions, n_0 incoming dislocations (with Burgers vector $\mathbf{b_0}$ gliding on plane $\mathbf{P_0}$ in matrix) are assumed to approach a $(11\bar{2}2)$ twin. As the dislocations react on a certain boundary, n_1 outgoing dislocations/TDs (with Burgers vector $\mathbf{b_1}$ gliding on plane $\mathbf{P_1}$) will be produced, and usually a residual dislocation $\mathbf{b^r}$ will be left at the interaction position. As for slip transmission and secondary twinning, the Burgers vector $\mathbf{b_1}$ and the plane $\mathbf{P_1}$ are defined in the twin crystal.

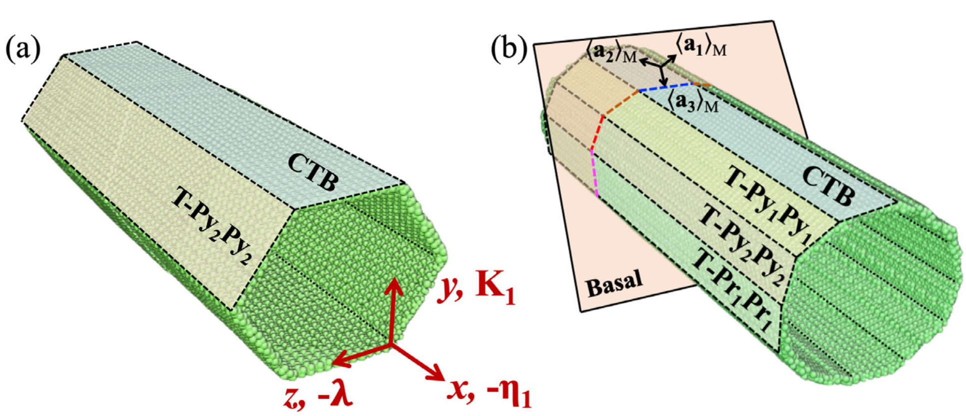

Fig. 2. (a) The unrelaxed model containing a $(11\bar{2}2)$ twin enclosed by CTB, T-Py_2Py_2 and T-Py_2Py_2' interfaces. (b) The relaxed model containing a $(11\bar{2}2)$ twin enclosed by CTB, T-Pr_1Pr_1/T-Pr_1Pr_1', T-Py_1Py_1/T-Py_1Py_1', and T-Py_2Py_2/T-Py_2Py_2' interfaces.

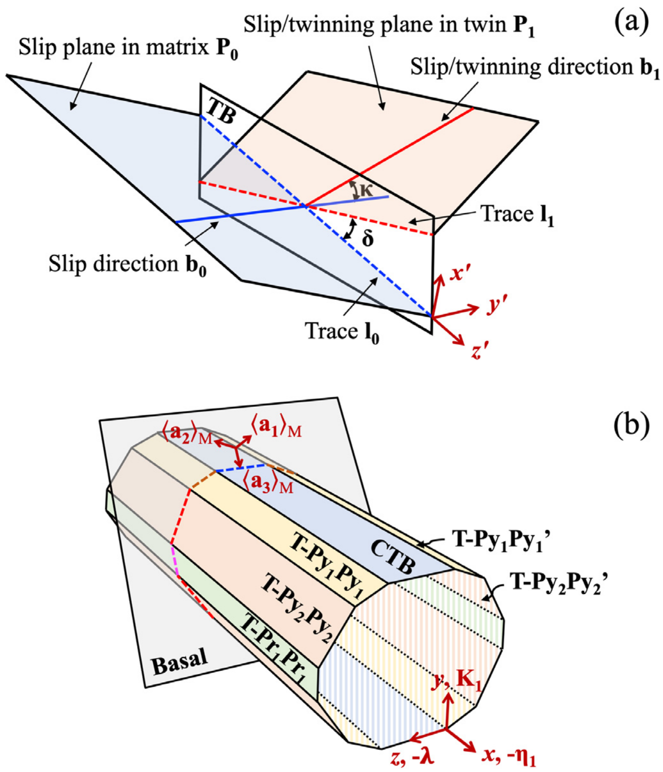

Fig. 3. Schematics showing (a) the misorientation between slip systems in matrix and slip/twinning systems in twin, and (b) traces on characteristic TBs as a dislocation on basal on basal plane loops the twin.

For twinning/detwinning of the primary twin, $\mathbf{b_1}$ is the Burgers vector of PTD ($\mathbf{b}_{tw}^{(11\bar{2}2)_M}$) and $\mathbf{P_1}$ is the twinning plane. All possible reactions are described in the form,

$$n_0\mathbf{b_0} \rightarrow n_1\mathbf{b_1} + \mathbf{b^r} \tag{1}$$

Werner's GM (Fig. 3(a)) [85] is adopted to evaluate the geometric slip continuity. The possibility is assessed by a parameter λ_m which is a function of the angle κ between $\mathbf{b_0}$ and $\mathbf{b_1}$, and the angle δ between $\mathbf{l_0}$ and $\mathbf{l_1}$ (where $\mathbf{l_0}$ is the trace of $\mathbf{P_0}$ on the TB and $\mathbf{l_1}$ is the trace of $\mathbf{P_1}$ on the TB).

$$\lambda_m = \cos\left(\frac{90^\circ}{\delta_c}\delta\right)\cos\left(\frac{90^\circ}{\kappa_c}\kappa\right) \tag{2}$$

where δ and κ are smaller than critical angles δ_c and κ_c [85]. The angle δ, representing the parallelism of two slip traces on the boundary, is more important than κ. δ_c is generally set as 15° [95]. The condition for angle κ can be less rigorous [85]. For Ti which has fewer deformation modes than the cubic crystals, the critical angle κ_c is set as 90° to avoid missing possible reactions. A modified form of Eq. (2) considering both Schmid factors of incoming and outgoing dislocations has been proposed by Beyerlein et al. [95]. Since we will discuss stress conditions later, here we apply Eq. (2) for the following analysis. For all possible reactions on/across TBs, the energy difference before and after a reaction is described as the change in elastic energy for the first order estimation, because dislocation core energy and formation energy of twins and so on are hard to estimate in crystallographic analysis. As the elastic energy associated with a dislocation is proportional to the square of the Burger vector [86], the change in elastic energy after the reaction is estimated as,

$$\Delta E = n_1\mathbf{b_1}^2 + \mathbf{b^r}^2 - n_0\mathbf{b_0}^2 \tag{3}$$

Following Frank's criteria [86], a negative ΔE indicates that the reaction is energetically favorable and likely takes place. A reaction with positive but small ΔE may happen under mechanical loading, but nucleation and emission of outgoing dislocations/TDs with large $\mathbf{b_1}$ are unlikely. It should be mentioned that the application of Werner's GM [85] and Frank's criteria [86] only indicates the possibility of a reaction, but does not guarantee it.

3.2. Classification of dislocation-twin interactions

We further classify the interactions with respect to the character of incoming dislocations, outgoing dislocations/TDs and the interaction TB. When $\langle\mathbf{a_i}\rangle$ (i = 1, 2, 3) dislocations either on the basal (0002) or prismatic $\{1\bar{1}00\}$ slip planes approach a twin, the possible interaction sites are considered to be the characteristic TBs. Fig. 3(b) shows the traces $\mathbf{l_0}$ on various TBs by dashed lines as a dislocation on basal plane loops the twin. Similarly, the traces on various TBs associated with a dislocation on prismatic plane can be identified. For the simplicity of the analysis using Eq. (2), we describe the Burgers vector in a local coordinate system as shown in Fig. 3(a), where the x'-axis is normal to the slip plane $\mathbf{P_0}$, z'-axis is along the trace $\mathbf{l_0}$, and y'-axis is the cross-product of z'- and x'-axis. Upon interacting, the line direction of an incoming dislocation is assumed to be parallel to $\mathbf{l_0}$. The edge component of the Burgers vector is thus along y'-axis while its screw component is along z'-axis. The edge and screw components are then normalized by the magnitude of the Burgers vector. Table 2 summarizes the normalized edge/screw components of Burgers vectors $\langle\mathbf{a_i}\rangle$ on various characteristic TBs. Correspondingly, four types of interactions are grouped for three slip vectors $\langle\mathbf{a_i}\rangle$ on (0002) or on the three $\{1\bar{1}00\}$ slip planes.

Type 1 is associated with basal $\langle\mathbf{a_3}\rangle$ dislocations that have edge character on CTB, screw character on T-Pr_1Pr_1, and mixed character on the other lateral-TBs. **Type 2** is associated with prismatic $\langle\mathbf{a_3}\rangle$ dislocations. These always have mixed character on all TBs. **Type 3** includes basal $\langle\mathbf{a_1}\rangle$ and $\langle\mathbf{a_2}\rangle$ dislocations. These have mirror symmetry about $(1\bar{1}00)$ plane (normal to $\boldsymbol{\lambda}$). As shown in Table 2, basal $\langle\mathbf{a_1}\rangle$ dislocations on CTB, T-Pr_1Pr_1, T-Py_1Py_1 and T-Py_2Py_2 have the same edge component, and the opposite screw component, as basal $\langle\mathbf{a_2}\rangle$ dislocations on CTB, T-Pr_1Pr_1, T-Py_1Py_1' and T-Py_2Py_2'. **Type 4** is associated with prismatic $\langle\mathbf{a_1}\rangle$ and $\langle\mathbf{a_2}\rangle$ dislocations sharing mirror symmetry about $(1\bar{1}00)$ plane (normal to $\boldsymbol{\lambda}$). It is found that basal $\langle\mathbf{a_1}\rangle$

Table 2
Character of dislocations on the TBs analyzed here. e/s represents edge/screw components in the local coordinate system, normalized by the magnitude of Burgers vector.

TB	Type 1 (e/s)	Type 2 (e/s)	Type 3 (e/s)		Type 4 (e/s)	
	Basal $\langle a_3\rangle$	Prism $\langle a_3\rangle$	Basal $\langle a_1\rangle$	Basal $\langle a_2\rangle$	Prism $\langle a_1\rangle$	Prism $\langle a_2\rangle$
CTB	−1.00/0.00	−0.85/0.53	0.50/−0.87	0.50/0.87	0.62/0.78	0.62/−0.78
T-Pr_1Pr_1	0.00/1.00	–	0.87/−0.50	0.87/−0.50	1.00/0.00	1.00/0.00
T-Py_1Py_1	−0.87/0.50	−0.85/0.53	0.00/−1.00	0.87/0.50	0.00/1.00	0.85/−0.53
T-Py_1Py_1'	−0.87/−0.50	−0.85/0.53	0.87/−0.50	0.00/1.00	0.85/0.53	0.00/−1.00
T-Py_2Py_2	−0.50/0.87	−0.85/0.53	−0.50/−0.87	1.00/0.00	−0.85/0.53	0.95/−0.30
T-Py_2Py_2'	−0.50/−0.87	−0.85/0.53	1.00/0.00	−0.50/0.87	0.95/0.30	−0.85/−0.53

and $\langle \mathbf{a_2} \rangle$ dislocations as well as prismatic $\langle \mathbf{a_1} \rangle$ and $\langle \mathbf{a_2} \rangle$ dislocations may have pure edge or pure screw character on some lateral-TBs.

We analyze the tendency of possible reactions associated with these four types of interactions using Werner's GM [85] and Frank's criteria [86]. In the analysis, $\langle \pm \mathbf{a_i} \rangle$ (i =1 or 3) dislocations either on basal or prismatic planes are considered, since dislocations with opposite sign can be activated under different stresses. Interaction sites are on characteristic TBs, including CTB, T-Pr$_1$Pr$_1$, T-Py$_1$Py$_1$, T-Py$_1$Py$_1$', T-Py$_2$Py$_2$ and T-Py$_2$Py$_2$' interfaces. Outgoing slip/twin systems considered in this analysis include basal $\langle \mathbf{a} \rangle$ slip, prismatic $\langle \mathbf{a} \rangle$ slip, 1st-order pyramidal $\langle \mathbf{a} \rangle$ and $\langle \mathbf{c+a} \rangle$ slip, and 2nd-order pyramidal $\langle \mathbf{c+a} \rangle$ slip in twin, as well as twinning/detwinning of primary $(11\bar{2}2)$ twinning by nucleation and glide of PTDs ($\mathbf{b}_{tw}^{(11\bar{2}2)_M}$) [90, 93, 96] on CTBs and secondary $\{\bar{1}012\}$ or $\{11\bar{2}1\}$ twinning via nucleation and glide of STDs ($\mathbf{b}_{tw}^{\{\bar{1}012\}_T}$ or $\mathbf{b}_{tw}^{\{11\bar{2}1\}_T}$).

Fig. 4 schematically displays possible reactions in 2D view where trace $\mathbf{l_0}$ is out of the paper. The top (in white color) and bottom (in gray color) regions represent matrix and twin. Dashed lines indicate slip trace on the viewed plane. In the matrix and twin, the outgoing dislocations/TDs (in dark red or blue color) are corresponding to the incoming dislocations in the same color. **Type 1** interactions are associated with basal $\langle \mathbf{a_3} \rangle$ and $\langle -\mathbf{a}_3 \rangle$ dislocations. Possible reactions including local twinning/detwinning of the primary twin, slip transmission and secondary twinning may take place on CTB (Fig. 4(a)), T-Py$_1$Py$_1$ and T-Py$_1$Py$_1$' (Fig. 4(c)). As shown in Fig. 4(a), $\langle \pm \mathbf{a_3} \rangle_M$ dislocations may dissociate into PTDs on CTB, causing local twinning/detwinning; $\langle \pm \mathbf{a_3} \rangle_M(0002)_M \rightarrow \langle \mp \mathbf{a_3} \rangle_T(0002)_T$ and $\langle \pm \mathbf{a_3} \rangle_M(0002)_M \rightarrow \langle \pm \mathbf{c} - \mathbf{a_3} \rangle_T(\bar{1}\bar{1}22)_T$ may take place since their associated δ is zero, λ_m is relatively large and ΔE is relatively small. Similarly, $(\bar{1}\bar{1}21)$ secondary twinning from CTB with zero δ and $(\bar{1}012)$ secondary twinning (Fig. 4(c)) from T-Py$_1$Py$_1$ with $\delta = 4.92\,^\circ$ likely happen since they have the largest λ_m and the most negative ΔE among their twin families.

Type 2 interactions are associated with prismatic $\langle \mathbf{a_3} \rangle$ and $\langle -\mathbf{a_3} \rangle$ dislocations. Possible reactions may take place on CTB (Fig. 4(e)), T-Py$_1$Py$_1$, T-Py$_1$Py$_1$', T-Py$_2$Py$_2$ and T-Py$_2$Py$_2$'. Local twinning/detwinning of the primary twin results from dissociation of $\langle \pm \mathbf{a_3} \rangle_M$ dislocations into PTDs. Slip transmission $\langle \pm \mathbf{a_3} \rangle_M(1\bar{1}00)_M \rightarrow \langle \mp \mathbf{a_3} \rangle_T(1\bar{1}00)_T$ likely happens because $(1\bar{1}00)_M$ and $(1\bar{1}00)_T$ slip planes are parallel. $(2\bar{1}\bar{1}1)$ and $(\bar{1}2\bar{1}1)$ secondary twinning also possibly happen because their $\mathbf{l_1}$ is parallel to $\mathbf{l_0}$, the associated λ_m is the largest and ΔE is the most negative.

Type 3 interactions are associated with basal $\langle \mathbf{a_1} \rangle$ and $\langle -\mathbf{a_1} \rangle$ dislocations. Possible reactions include local twinning/detwinning of the primary twin, slip transmission and secondary twinning. The associated reactions may take place on CTB (Fig. 4(a)), T-Pr$_1$Pr$_1$ (Fig. 4(b)), T-Py$_1$Py$_1$ (Fig. 4(c)) and T-Py$_2$Py$_2$ (Fig. 4(d)). Local twining/detwinning may take place on CTB. Slip transmission $\langle \pm \mathbf{a_1} \rangle_M(0002)_M \rightarrow \langle \mp \mathbf{a_1} \rangle_T(0002)_T$ (with $\delta = 0\,^\circ$ on CTB) and $\langle \pm \mathbf{a_1} \rangle_M(0002)_M \rightarrow \langle \mp \mathbf{a_1} \rangle_T(01\bar{1}0)_T$ (with $\delta = 7.46\,^\circ$ on T-Py$_2$Py$_2$) probably take place since their associated λ_m is relatively large while ΔE is positive but relatively small. $(\bar{2}111)$ (with $\delta = 6.70\,^\circ$ on T-Pr$_1$Pr$_1$) and $(\bar{1}012)$ (with $\delta = 4.92\,^\circ$ on T-Py$_2$Py$_2$) secondary twinning are more likely happening among their twin families because they have the largest λ_m and the most negative ΔE.

Type 4 interactions are associated with prismatic $\langle \mathbf{a_1} \rangle$ and $\langle -\mathbf{a_1} \rangle$ dislocations. Possible reactions take place on CTB (Fig. 4(f)), T-Py$_1$Py$_1$' (Fig. 4(g)) and T-Py$_2$Py$_2$ (Fig. 4(h)). Local twinning/detwinning of the primary twin may happen via dissociation of $\langle \pm \mathbf{a_1} \rangle_M$ dislocations into PTDs. Meanwhile, slip transmission $\langle \pm \mathbf{a_1} \rangle_M(01\bar{1}0)_M \rightarrow \langle \pm \mathbf{a_2} \rangle_T(\bar{1}010)_T$ (with $\delta = 0\,^\circ$ on CTB) and $\langle \pm \mathbf{a_1} \rangle_M(01\bar{1}0)_M \rightarrow \langle \mp \mathbf{a_1} \rangle_T(0002)_T$ (with $\delta = 7.46\,^\circ$ on T-Py$_2$Py$_2$) probably take place since their

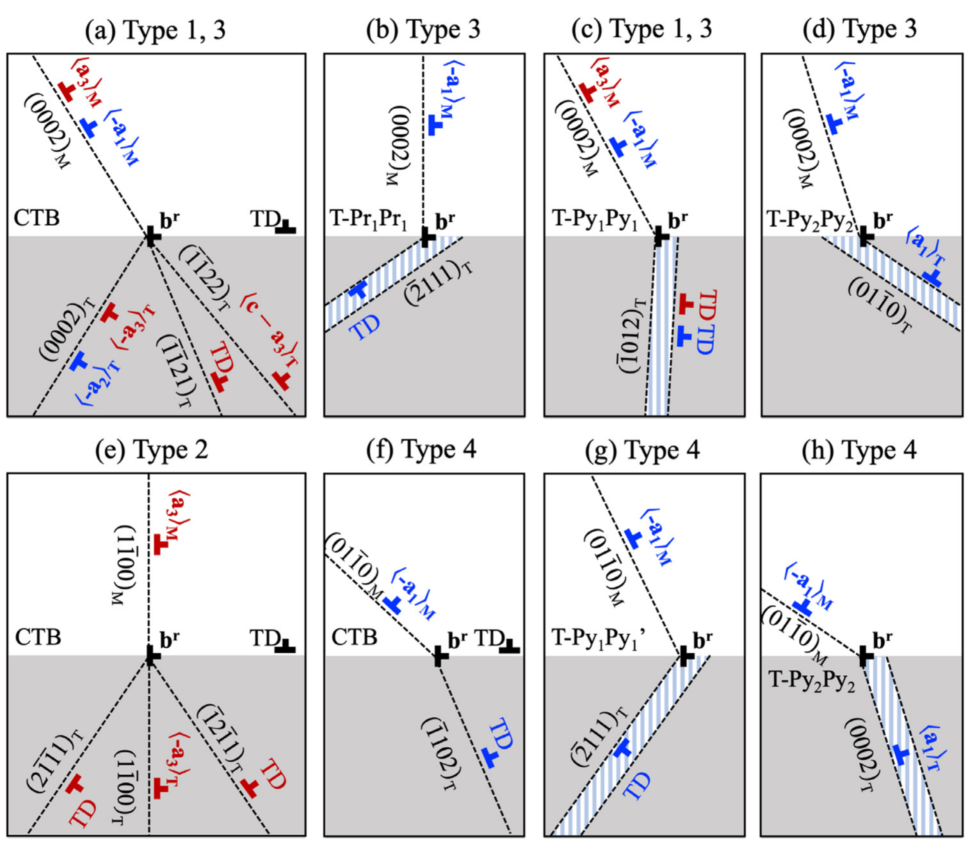

Fig. 4. Possible reactions involving incoming $\langle \mathbf{a_i} \rangle_M$ (i = 1, 2, 3) dislocation on $(0002)_M$ planes on (a) CTB, (b) T-Pr$_1$Pr$_1$, (c) T-Py$_1$Py$_1$ and (d) T-Py$_2$Py$_2$. (e) Possible reactions involving incoming $\langle \mathbf{a_3} \rangle_M$ dislocation on $(1\bar{1}00)_M$ planes on CTB. Possible reactions involving incoming $\langle \mathbf{a_i} \rangle_M$ dislocation on $(01\bar{1}0)_M$ planes on (f) CTB, (g) T-Py$_1$Py$_1$' and (h) T-Py$_2$Py$_2$. (Shaded area shows slip planes that are not edge-on in current view.)

Table 3
Possible reactions associated with **type 1**–**4** interaction. Refer to Fig. 4 for complementary information. The Burgers vector of the residual dislocation has a complex form and is not listed in the Table.

$\mathbf{b_1}$	$\mathbf{P_1}$	κ (°)	δ (°)/TB	λ_m	n_0	n_1	ΔE (Å^2)
Type 1: $\mathbf{b_0}$: $\langle \mathbf{a_3} \rangle_M$; $\mathbf{P_0}$: $(0002)_M$							
$\mathbf{b}_{tw}^{(11\bar{2}2)_M}$	$(11\bar{2}2)_M$	57.77	0/CTB	0.53	1	−5	−2.06
$\langle -\mathbf{a_3} \rangle_T$	$(0002)_T$	64.47	0/CTB	0.43	1	1	9.92
$\langle \mathbf{c}-\mathbf{a_3} \rangle_T$	$(\bar{1}\bar{1}22)_T$	6.70	0/CTB	0.99	2	1	13.78
$\mathbf{b}_{tw}^{(\bar{1}012)_T}$	$(\bar{1}012)_T$	27.79	4.92/T-Py_1Py_1	0.77	1	4	−5.30
$\mathbf{b}_{tw}^{(0\bar{1}12)_T}$	$(0\bar{1}12)_T$	27.79	4.92/T-Py_1Py_1’	0.77	1	4	−5.30
$\mathbf{b}_{tw}^{(\bar{1}\bar{1}21)_T}$	$(\bar{1}\bar{1}21)_T$	8.03	0/CTB	0.99	1	9	−7.69
Type 2: $\mathbf{b_0}$: $\langle \mathbf{a_3} \rangle_M$; $\mathbf{P_0}$: $(1\bar{1}00)_M$							
$\mathbf{b}_{tw}^{(11\bar{2}2)_M}$	$(11\bar{2}2)_M$	57.77	0/CTB	0.53	1	−5	−2.06
$\langle -\mathbf{a_3} \rangle_T$	$(1\bar{1}00)_T$	64.47	0/CTB; T-Py_1Py_1; T-Py_1Py_1’; T-Py_2Py_2; T-Py_2Py_2’	0.43	1	1	9.92
$\mathbf{b}_{tw}^{(2\bar{1}\bar{1}1)_T}$	$(2\bar{1}\bar{1}1)_T$	37.27	0/CTB; T-Py_1Py_1; T-Py_1Py_1’; T-Py_2Py_2	0.80	1	7	−4.83
$\mathbf{b}_{tw}^{(\bar{1}2\bar{1}1)_T}$	$(\bar{1}2\bar{1}1)_T$	37.27	0/CTB; T-Py_1Py_1; T-Py_1Py_1’; T-Py_2Py_2’	0.80	1	7	−4.83
Type 3: $\mathbf{b_0}$: $\langle \mathbf{a_1} \rangle_M$; $\mathbf{P_0}$: $(0002)_M$							
$\mathbf{b}_{tw}^{(11\bar{2}2)_M}$	$(11\bar{2}2)_M$	74.53	0/CTB	0.27	1	2	−0.41
$\langle -\mathbf{a_1} \rangle_T$	$(0002)_T$	30.94	0/CTB	0.86	1	1	2.48
$\langle -\mathbf{a_1} \rangle_T$	$(01\bar{1}0)_T$	30.94	7.46/T-Py_2Py_2	0.61	1	1	2.48
$\mathbf{b}_{tw}^{(\bar{1}012)_T}$	$(\bar{1}012)_T$	40.39	4.92/T-Py_1Py_1	0.66	−1	3	−3.76
$\mathbf{b}_{tw}^{(\bar{2}111)_T}$	$(\bar{2}111)_T$	46.51	6.70/T-Pr_1Pr_1	0.53	−1	6	−3.54
Type 4: $\mathbf{b_0}$: $\langle \mathbf{a_1} \rangle_M$; $\mathbf{P_0}$: $(01\bar{1}0)_M$							
$\mathbf{b}_{tw}^{(11\bar{2}2)_M}$	$(11\bar{2}2)_M$	74.53	0/CTB	0.27	1	2	−0.41
$\langle \mathbf{a_1} \rangle_M$	$(\bar{1}010)_T$	50.04	0/CTB	0.64	1	1	6.23
$\langle -\mathbf{a_1} \rangle_T$	$(0002)_T$	30.94	7.46/T-Py_2Py_2	0.61	1	1	2.48
$\mathbf{b}_{tw}^{(11\bar{2}2)_M}$	$(11\bar{2}2)_M$	74.53	0/CTB	0.27	1	2	−0.41
$\mathbf{b}_{tw}^{(\bar{1}102)_T}$	$(\bar{1}102)_T$	19.37	0/CTB	0.94	−1	4	−6.15
$\mathbf{b}_{tw}^{(\bar{2}111)_T}$	$(\bar{2}111)_T$	46.51	7.74/T-Py_1Py_1’	0.69	−1	6	−3.54

associated λ_m is relatively large while ΔE is positive but relatively small. $(\bar{1}102)$ secondary twinning from CTB with zero δ and $(\bar{2}111)$ secondary twinning from T-Py_1Py_1’ with $\delta = 7.74$ ° likely happen since they have the largest λ_m and the most negative ΔE among their families.

Table 3 summarizes possible reactions in Fig. 4 and lists all parameters. n_0 and n_1 are the number of $\mathbf{b_0}$ and $\mathbf{b_1}$ dislocations that can produce the smallest ΔE. The signs of n_0 and n_1 indicate a change in the direction of Burgers vectors. Local growth of the primary twin takes place when n_1 is positive while detwinning occurs when n_1 is negative.

3.3. Remarks

The analysis presented above is unavoidably complex but necessary to establish a complete set of *possible* dislocation reactions at twin facets. The analysis provides a hint as to which ones *may* be favorable, although it does not provide certainty about the reactions that will *actually* take place. Once characteristic TBs of the 3D twin are considered as interaction sites, the combined application of Werner’s GM [85] and Frank’s criteria [86] makes it possible to identify dislocation-twin reactions that cannot be inferred from CMR. From a thermodynamics perspective, all reactions may take place, with a likelihood that depends on the energy and kinetics of defects involved in the reaction. In crystallographic analysis, Werner’s GM [85] takes care of geometric compatibility and Frank’s criteria deals with the change in elastic energy. It is noted that when secondary twinning is a product of the reaction, it has the largest λ_m and the most negative ΔE in all four types of interactions. In this sense, when the kinetics is not accounted for in the analysis, one would conclude that secondary twinning is more likely to happen during all types of interactions. However, the likelihood of possible reactions may vary with other factors such as dislocation core energy, formation energy of twins (elastic and interfacial), kinetics associated with dislocations and twins, and stress. Therefore, the only way to examine these potential reactions and to decide their feasibility is by performing MD simulations. In what follow we present the results of such approach. For each configuration in Fig. 4 the applied loading is preselected according to crystallographic analysis in order to facilitate a specific reaction.

4. Atomistic simulations

The construction of simulation models for interactions between $\langle \mathbf{a} \rangle$ dislocations and a $(11\bar{2}2)$ twin starts with the relaxed twin model shown in Fig. 2(b). Dislocations with Burgers vector $\langle \pm \mathbf{a_i} \rangle$ (i =1 or 3) on basal or prismatic plane in matrix are introduced into the model at 2 nm separation from the TB with the application of the anisotropic Barnett-Lothe solution [92] for the displacement field of a dislocation. Using the EAM potential developed by Zope and Mishin [91], the models are then relaxed for 20 ps at 10 K in the absence of applied stress. For MD simulations of **type 1** and **3** interactions, the introduction of $\langle \mathbf{a} \rangle$ dislocations on basal planes breaks the periodicity in x-direction. So, periodic boundary condition is applied along the z-axis while a 1 nm region adjacent to the surfaces normal to x- and y-directions is fixed. For simulations of **type 2** interactions, there is no periodicity along the z-direction after the introduction of $\langle \mathbf{a_3} \rangle_M$ dislocations on $(1\bar{1}00)_M$ planes. During relaxation, periodic boundary conditions are applied along x-axis while a 1 nm region adjacent to the surfaces normal to y- and z-directions is fixed. For simulations of **type 4** interactions, a 1 nm region adjacent to the surface normal to x-, y- and z-

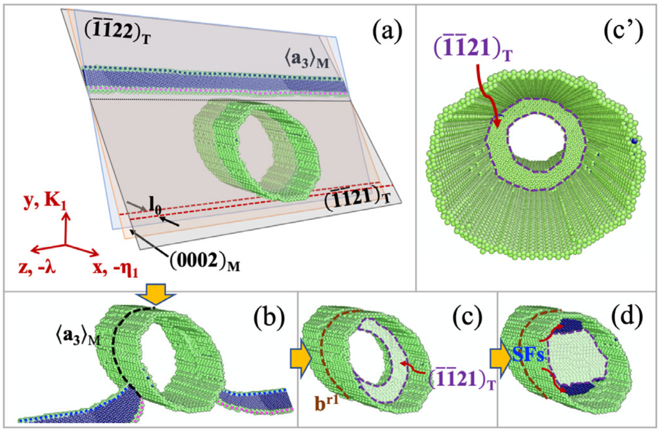

Fig. 5. (a) Initial configuration containing an $\langle \mathbf{a_3} \rangle_M$ dislocation on $(0002)_M$ plane and a $(11\bar{2}2)$ twin. (b) The $\langle \mathbf{a_3} \rangle_M$ dislocation loops the twin. (c) Ring-shaped $(\bar{1}\bar{1}21)$ secondary twin nucleates around inner boundary of the primary twin. (c') The view of structure in (c) along $\boldsymbol{\eta_1}$ direction. (d) Formation of one secondary twin and two I2 SFs.

directions is fixed since periodicity in all dimensions breaks after the introduction of $\langle \mathbf{a_1} \rangle_M$ dislocations. Later on, a stress tensor will be applied to the models to drive the $\langle \mathbf{a} \rangle$ dislocations towards the twin. It takes 2 ps to increase the stress tensor from zero to a constant value. To trigger possible reactions on/across TBs, the applied stress tensor is designed to produce a large resolved shear stress (RSS) on the dislocation or twinning associated with those reactions.

4.1. Type 1 interactions: $\langle \mathbf{a_3} \rangle_M (0002)_M \rightarrow \left(\bar{1}\bar{1}21\right)$ secondary twinning

The possible reactions associated with **type 1** interactions are schematically shown in Fig. 4(a) and (c). Crystallographic analysis (in Table 3) suggests that slip transmission, twinning/detwinning of the primary twin and secondary tensile twinning may occur as $\langle \mathbf{a_3} \rangle_M$ dislocations on $(0002)_M$ planes interact with the twin. In addition, secondary twinning can be ruled out when the opposite dislocation $\langle -\mathbf{a_3} \rangle_M$ on the $(0002)_M$ plane interacts with the twin. Slip transmission $\langle \pm \mathbf{a_3} \rangle_M (0002)_M \rightarrow \langle \pm \mathbf{c} - \mathbf{a_3} \rangle_T \left(\bar{1}\bar{1}22\right)_T$ and $(\bar{1}\bar{1}21)$ secondary twinning induced by $\langle \mathbf{a_3} \rangle_M$ dislocations are of great likelihood because their λ_m is close to 1. Meanwhile, $(\bar{1}\bar{1}21)$ secondary twinning produces the most negative ΔE. It should be noted that two $\langle \mathbf{a_3} \rangle_M$ dislocations are needed to produce one $\langle \mathbf{c} - \mathbf{a_3} \rangle_T$ dislocation. In what follows, we show interactions where one or two $\langle \pm \mathbf{a_3} \rangle_M$ dislocations on one $(0002)_M$ plane approach the twin, revealing the formation of $(\bar{1}\bar{1}21)$ secondary twins.

Fig. 5(a) shows an incoming $\langle \mathbf{a_3} \rangle_M$ dislocation on $(0002)_M$ plane. The line direction of the incoming dislocation is along the z-axis. The dislocation has a planar extended core structure and consists of two mixed partial dislocations (pink and dark blue dot lines) and an I2 stacking fault (SF) in-between. The two partial dislocations have the same edge components and opposite screw components. The black dotted line shows the intersection line between the $(0002)_M$ gliding plane and the upper CTB. It is noted that $(\bar{1}\bar{1}22)_T$ gliding plane and $(\bar{1}\bar{1}21)_T$ twinning plane share the same intersection line along the black dotted line. To promote the reaction, we apply a stress tensor $\boldsymbol{\sigma_1}$,

$$\boldsymbol{\sigma_1} = \begin{pmatrix} 0.75 & 0 & 0 \\ 0 & -0.3 & 0 \\ 0 & 0 & 0 \end{pmatrix} \text{GPa} \tag{4}$$

that produces a 0.47 GPa RSS on the incoming $\langle \mathbf{a_3} \rangle_M$ dislocation on $(0002)_M$ plane, 0.41 GPa RSS on an outgoing $\langle \mathbf{c} - \mathbf{a_3} \rangle_T$ dislocation on $(\bar{1}\bar{1}22)_T$ plane, 0.51 GPa RSS associated with the $(\bar{1}\bar{1}21)$ secondary twinning, and zero RSS associated with twinning/detwinning of the primary twin.

The 3D view of the interaction process is shown in **movie 1**, and the corresponding cross-section view normal to $\boldsymbol{\lambda}$ direction is shown in **movie 2**. As shown in Fig. 5(b), the incoming $\langle \mathbf{a_3} \rangle_M$ dislocation loops around the twin. The looping part of the dislocation has a condensed core structure. After looping, an $\langle \mathbf{a_3} \rangle_M$ dislocation loop is left around the twin. As shown in Fig. 5(c), the interaction between the dislocation loop and TBs results in the activation of a $(\bar{1}\bar{1}21)$ secondary twin around the inner boundary of the primary twin, forming a ring-shaped twin domain (Fig. 5(c')). Such reaction can be expressed as,

$$\langle \mathbf{a_3} \rangle_M \rightarrow n_1 \mathbf{b}_{tw}^{(\bar{1}\bar{1}21)_T} + \mathbf{b}^{r1} \tag{5}$$

The crystallographic analysis suggests that the reaction is favored because of the small angles κ and δ (less than 10°). In addition, $n_1 = 9$

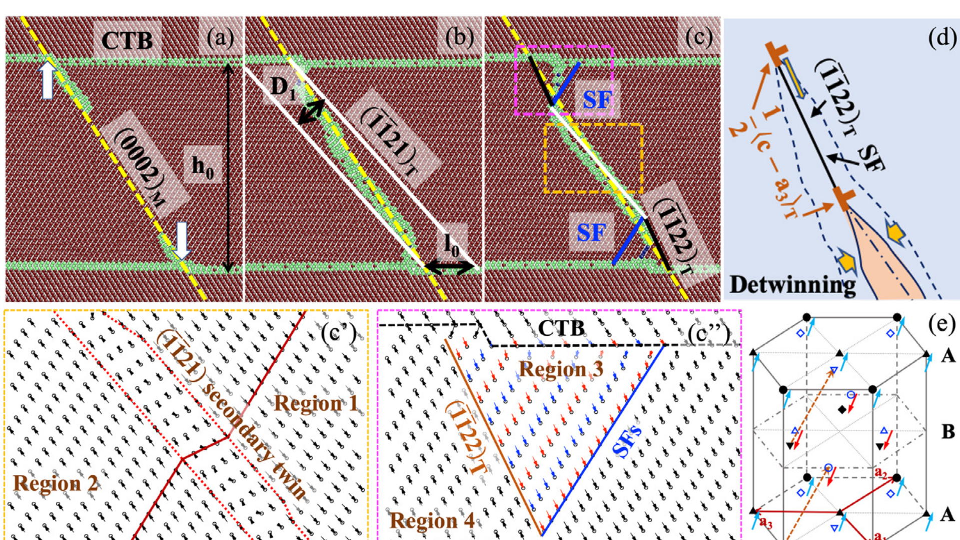

Fig. 6. Cross-section views normal to λ direction showing (a) nucleation of $(\bar{1}\bar{1}21)$ secondary twins on the upper and lower CTBs. (b) coalescence of two secondary twins into a twin with an irregular shape. (c) detwinning of the irregular-shaped secondary twin accompanied by emission of partial dislocations from secondary twin tips. Atom displacements in region enclosed by (c') orange square and (c'') pink square in (c). (d) Schematics illustrating secondary detwinning together with glide of one $\frac{1}{2}\langle \mathbf{c} - \mathbf{a_3} \rangle_T$ partial dislocation on $(\bar{1}\bar{1}22)_T$ plane. (e) A unit cell of HCP structure. Symbols of atoms represent different position along $[1\bar{1}00]_T$ direction. After a rigid displacement of $\frac{1}{2}\langle \mathbf{c} - \mathbf{a_3} \rangle$, black atoms are moved to positions where blue atoms are.

minimizes the elastic energy change. Fig. 5(d) shows a whole secondary twin which develops from the ring-shaped twin domain, and I2 SFs that form between the tips of the secondary twin and TBs of the primary twin.

Fig. 6(a)-(c) reveals details of the formation of the secondary twin. As the incoming dislocation loops the twin, reactions take place on the upper and lower CTBs. In Fig. 6(a), the yellow dashed line marks the position of the $(0002)_M$ gliding plane. Two white arrows mark the nucleation sites of the secondary twin on CTBs, which are also the intersection lines between the $(0002)_M$ gliding plane and CTBs. Fig. 6 (a) shows local shears (corresponding to the nucleation of a ring-shaped twin) in the primary twin due to the incoming dislocation. The two white solid lines represent two $(\bar{1}\bar{1}21)_T$ planes with a separation D_1. Considering that the height of the primary twin is $h_0 = 10.50$ nm, the angle between $(0002)_M$ plane and CTB is $\alpha = 57.76°$, and the angle between $(\bar{1}\bar{1}21)_T$ plane and CTB is $\beta = 49.79°$, then $D_1 = \left(\frac{h}{\tan\beta} - \frac{h}{\tan\alpha}\right)\sin\beta = 1.72$ nm and spans 24 $\{11\bar{2}1\}$ atomic planes. The distance D_1 is much larger than the thickness of the secondary twins. When secondary twins propagate and coalesce, a whole twin forms having an irregular shape (Fig. 6(b)).

The irregular shape of the secondary twin further transforms into a lenticular shape, as shown in Fig. 6(c). The secondary twin tips and the nucleation sites are always connected by $(\bar{1}\bar{1}22)_T$ planes (black solid lines). Successive emission of partial dislocations on $(0002)_T$ planes takes place during the transformation. To identify the displacements of atoms within the transformation regions, we choose two representative regions identified by dashed squares. The orange square outlines $(\bar{1}\bar{1}21)$ secondary twinning region, and the associated atom displacements are plotted in Fig. 6(c'). The region enclosed by the pink square undergoes $(\bar{1}\bar{1}21)$ secondary twinning followed by detwinning accompanied with successive glide of partial dislocations on $(0002)_T$ planes. The atomic displacements are plotted in Fig. 6(c''). In Fig. 6(c') and (c''), arrows show the in-plane displacement normal to $\boldsymbol{\lambda}$ direction while the colors reveal the out-of-plane displacement parallel to $\boldsymbol{\lambda}$ direction (−0.17 nm for blue arrows, 0 nm for green arrows, and 0.17 nm for red arrows).

Fig. 6(c') displays a seven-layer secondary twin. Across the secondary twin, region 1 undergoes a relative shear along $[11\bar{2}6]_T$ direction with a magnitude of 0.31 nm (which is equal to $7\mathbf{b}_{\mathbf{tw}}^{(\bar{1}\bar{1}21)_T}$) with respect to region 2. The number of STDs ($n_1 = 7$) is slightly smaller than $n_1 = 9$ predicted by crystallographic analysis.

Fig. 6(c'') displays the region after secondary detwinning followed by emission and glide of partial dislocations on basal planes. Region 3, separated by a $(\bar{1}\bar{1}22)_T$ plane from region 4, shows relative $\frac{1}{2}\langle\mathbf{c}-\mathbf{a_3}\rangle_T$ shear. As suggested by the atomic displacements, Fig. 6(d) is proposed to schematically describe the detwinning process (from the domain enclosed by dashed line to the orange domain). A $\frac{1}{2}\langle\mathbf{c}-\mathbf{a_3}\rangle_T$ partial dislocation glides on $(\bar{1}\bar{1}22)_T$ plane, and is always on the tip of the secondary twin. Consequently, a SF on the $(\bar{1}\bar{1}22)_T$ plane is created. The SF is then corrected by the successive glide of screw partial dislocations on every $(0002)_T$ plane in region 3. The correction of the SF is illustrated in Fig. 6(e). It shows an HCP unit cell with ...ABAB... stacking. In the cell, blue open atoms undergo a $\frac{1}{2}\langle\mathbf{c}-\mathbf{a_3}\rangle_T$ shift (brown arrows) with respect to black solid atoms. On A- and B-layers, blue open atoms can move to black solid atoms by vectors $\frac{1}{6}[\bar{1}100]$ (light blue arrows on A-layers) and $\frac{1}{6}[1\bar{1}00]$ (red arrows on B-layers). This operation can be accomplished by successive glide of $\pm\frac{1}{3}[1\bar{1}00]$ partial dislocations on every basal plane, creating an I2 SF. The correction of the SF on $(\bar{1}\bar{1}22)_T$ plane is energetically favorable since I2 SF has lower SF energy than a SF on $\{11\bar{2}2\}$ plane [97].

$(\bar{1}\bar{1}21)$ secondary twinning takes place but no $\langle\mathbf{c}-\mathbf{a_3}\rangle_T$ dislocation is activated although the applied loading can generate 0.41 GPa RSS on an outgoing $\langle\mathbf{c}-\mathbf{a_3}\rangle_T$ dislocation on $(\bar{1}\bar{1}22)_T$ plane and 0.51 GPa RSS associated with $(\bar{1}\bar{1}21)$ secondary twinning. For the same geometry, we apply another stress tensor that produces 0.50 GPa RSS associated with twinning/detwinning of the primary twin and 0.51 GPa RSS associated with $(\bar{1}\bar{1}21)$ secondary twinning. Again, secondary twinning takes place while twinning/detwinning of primary twin does not. In other words, the reaction does not create 3-layer TDs of $(11\bar{2}2)$ twinning.

The interaction discussed above between two $\langle\mathbf{a_3}\rangle_M$ dislocations on $(0002)_M$ plane and a $(11\bar{2}2)$ twin under the stress tensor $\boldsymbol{\sigma_1}$ is shown in **movie 3** in 3D view and **movie 4** in cross-section view. As shown in Fig. 7(a), a $(\bar{1}\bar{1}21)$ secondary twin nucleates from the upper CTB before the 1st incoming dislocation fully loops the twin. The secondary twin further propagates and reaches the lower CTB as shown

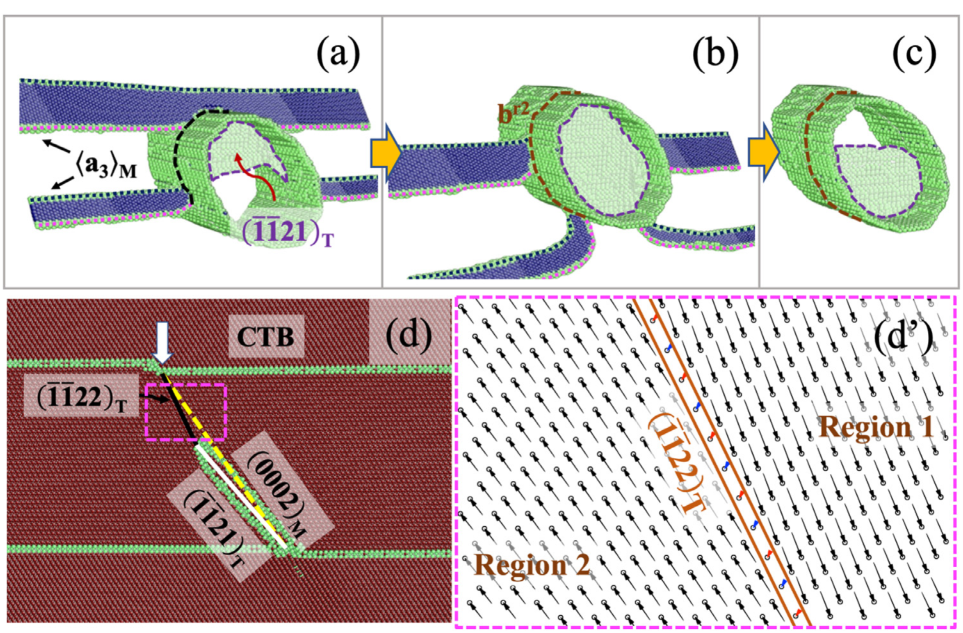

Fig. 7. During interaction between two $\langle\mathbf{a_3}\rangle_M$ dislocations on $(0002)_M$ plane and a $(11\bar{2}2)$ twin: (a) $(\bar{1}\bar{1}21)$ secondary twin nucleates from the upper CTB before the 1st $\langle\mathbf{a_3}\rangle_M$ dislocation fully loops the twin. (b) The secondary twin reaches the lower TB. (c) Detwinning of the secondary twin. (d) Cross-section view normal to λ direction of (c). (d') Atom displacements in region enclosed by pink square in (d).

in Fig. 7(b). Then, secondary detwinning takes place from the upper CTB as shown in Fig. 7(c). In this case, secondary detwinning still happens even though it has a lenticular shape. Fig. 7(d) shows the corresponding cross-section view normal to $\boldsymbol{\lambda}$ direction of Fig. 7(c). We choose one representative region enclosed by pink dashed squares to reveal atom displacements after secondary detwinning. In Fig. 7(d'), arrows show the in-plane displacement normal to $\boldsymbol{\lambda}$ direction while the colors reveal the out-of-plane displacement parallel to $\boldsymbol{\lambda}$ direction (−0.17 nm for blue arrows, 0 nm for green arrows, and 0.17 nm for red arrows). Regions 1 and 2 are on each side of a $(\bar{1}\bar{1}22)_T$ layer (bounded by two orange solid lines). Region 1 undergoes a relative displacement which is $\langle \mathbf{c}-\mathbf{a_3}\rangle_T$, with respect to region 2. There is no in-plane displacement on the $(\bar{1}\bar{1}22)_T$ layer, indicating that the $\langle \mathbf{c}-\mathbf{a_3}\rangle_T$ shear is accomplished by two $\frac{1}{2}\langle \mathbf{c}-\mathbf{a_3}\rangle_T$ shears on two neighboring $(\bar{1}\bar{1}22)_T$ planes. This operation creates two SFs on two neighboring $(\bar{1}\bar{1}22)_T$ planes, which are corrected by the out-of-plane shuffling of atoms on the $(\bar{1}\bar{1}22)_T$ layer. This mechanism likely helps stress relaxation inside the twin.

We also simulate the interaction involving two $\langle$-$\mathbf{a_3}\rangle_M$ dislocations. In this case neither secondary twinning, nor activation of $\langle \mathbf{c}-\mathbf{a_3}\rangle_T$ on $(\bar{1}\bar{1}22)_T$ plane, nor twinning/detwinning of the primary twin take place.

4.2. Type 2 interactions: $\langle \pm \mathbf{a_3}\rangle_M \left(1\bar{1}00\right)_M \rightarrow \langle \mp \mathbf{a_3}\rangle_T \left(1\bar{1}00\right)_T$

Possible reactions associated with **type 2** interactions (in Table 3) are schematically shown in Fig. 4(e). Slip transmission, twinning/detwinning of the primary twin and secondary tensile twinning may occur as $\langle \mathbf{a_3}\rangle_M$ dislocations on the $(1\bar{1}00)_M$ plane interact with the twin, but secondary twinning is ruled out when $\langle$-$\mathbf{a_3}\rangle_M$ dislocations on $(1\bar{1}00)_M$ plane approach the twin. Of all possible reactions that may take place on the CTB, $(2\bar{1}\bar{1}1)$ and $(\bar{1}2\bar{1}1)$ secondary twinning has the largest λ_m and most negative ΔE, but slip transmission $\langle \pm \mathbf{a_3}\rangle_M \left(1\bar{1}00\right)_M \rightarrow \langle \mp \mathbf{a_3}\rangle_T \left(1\bar{1}00\right)_T$ has smaller λ_m and larger ΔE. All these reactions may be activated regardless of the sign of $\langle \mathbf{a_3}\rangle_M$ dislocation.

Fig. 8(a) shows the model with an incoming $\langle \mathbf{a_3}\rangle_M$ dislocation on $(1\bar{1}00)_M$ plane. The $\langle \mathbf{a_3}\rangle_M$ dislocation has a planar core. With its line direction along x-axis, the $\langle \mathbf{a_3}\rangle_M$ dislocation has mixed character. To promote $(2\bar{1}\bar{1}1)$ secondary twinning, we apply a stress tensor $\boldsymbol{\sigma_2}$,

$$\boldsymbol{\sigma_2} = \begin{pmatrix} 0 & 0 & 1.50 \\ 0 & 0 & -1.00 \\ 1.50 & -1.00 & 0 \end{pmatrix} \text{GPa} \tag{6}$$

that produces 1.65 GPa RSS on the incoming $\langle \mathbf{a_3}\rangle_M$ dislocation on $(1\bar{1}00)_M$ plane, 1.27 GPa RSS associated with $(2\bar{1}\bar{1}1)$ secondary twinning, and 0.05 GPa RSS on an outgoing $\langle$-$\mathbf{a_3}\rangle_T$ dislocation on $(1\bar{1}00)_T$ plane. MD simulations show that the $\langle \mathbf{a_3}\rangle_M$ dislocation is obstructed by the twin and no reactions are observed. To promote slip transmission of a $\langle \mathbf{a_3}\rangle_M$ dislocation into twin, we apply a stress tensor $\sigma_2{}'$,

$$\boldsymbol{\sigma_2}' = \begin{pmatrix} 0 & -1.00 & 0 \\ -1.00 & 0 & -1.50 \\ 0 & -1.50 & 0 \end{pmatrix} \text{GPa} \tag{7}$$

that produces 1.27 GPa RSS on the incoming $\langle \mathbf{a_3}\rangle_M$ dislocation on $(1\bar{1}00)_M$ plane, 1.27 GPa RSS on an outgoing $\langle$-$\mathbf{a_3}\rangle_T$ dislocation on $(1\bar{1}00)_T$ plane, 0.25 GPa RSS associated with $(2\bar{1}\bar{1}1)$ or $(\bar{1}2\bar{1}1)$ secondary twinning, and 1.00 GPa RSS associated with twinning/detwinning of the primary twin. The interaction process is shown in **movie 5** in 3D view. As shown in Fig. 8(b) and (c), the $\langle \mathbf{a_3}\rangle_M$ dislocation induces a $\langle$-$\mathbf{a_3}\rangle_T$ dislocation on $(1\bar{1}00)_T$ plane inside the twin, which eventually transmits into the matrix, inducing a $\langle \mathbf{a_3}\rangle_M$ dislocation on $(1\bar{1}00)_M$ plane. Two residual dislocations $\mathbf{b^{r2}}$ and -$\mathbf{b^{r2}}$ are left on the upper and bottom TBs. The reaction can be expressed as,

$$\langle \mathbf{a_3}\rangle_M \rightarrow \langle -\mathbf{a_3}\rangle_T + \mathbf{b^{r2}} \text{ and } \langle -\mathbf{a_3}\rangle_T \rightarrow \langle \mathbf{a_3}\rangle_M - \mathbf{b^{r2}} \tag{8}$$

The incoming $\langle \mathbf{a_3}\rangle_M$ dislocation and the outgoing $\langle$-$\mathbf{a_3}\rangle_T$ dislocation have the same edge component and opposite screw component. Consequently, the residual dislocation $\mathbf{b^{r2}}$ has Burgers vector (0.316, 0, 0) nm, and is of screw character. Fig. 8(d) shows possible slip planes with their co-zone parallel to the line direction of residual dislocation $\mathbf{b^{r2}}$. On each slip plane, the dashed line represents the dislocation line, while the arrow shows the Burgers vectors. A pure screw $\langle \mathbf{c}+\mathbf{a_3}\rangle_T$ dislocation which is around 1.75$\mathbf{b^{r2}}$ may glide on $(10\bar{1}1)_T$ and $(01\bar{1}1)_T$ planes. With successive $\langle \mathbf{a_3}\rangle_M$ dislocations gliding on the $(1\bar{1}00)_M$ plane and transmitting into the twin as $\langle$-$\mathbf{a_3}\rangle_T$ dislocations, residual dislocations $\mathbf{b^{r2}}$ accumulate and may cross-slip onto $(10\bar{1}1)_T$ and $(01\bar{1}1)_T$ planes as $\langle \mathbf{c}+\mathbf{a_3}\rangle_T$ dislocations to reduce total elastic energy. During the interaction, twinning/detwinning of the primary twin is not observed. We further simulate the interaction between an incoming $\langle$-$\mathbf{a_3}\rangle_M$ dislocation on $(1\bar{1}00)_M$ plane and a $(11\bar{2}2)$ twin under stress tensor -$\boldsymbol{\sigma_2}'$. A similar reaction $\langle -\mathbf{a_3}\rangle_M \rightarrow \langle \mathbf{a_3}\rangle_T - \mathbf{b^{r2}}$ takes place.

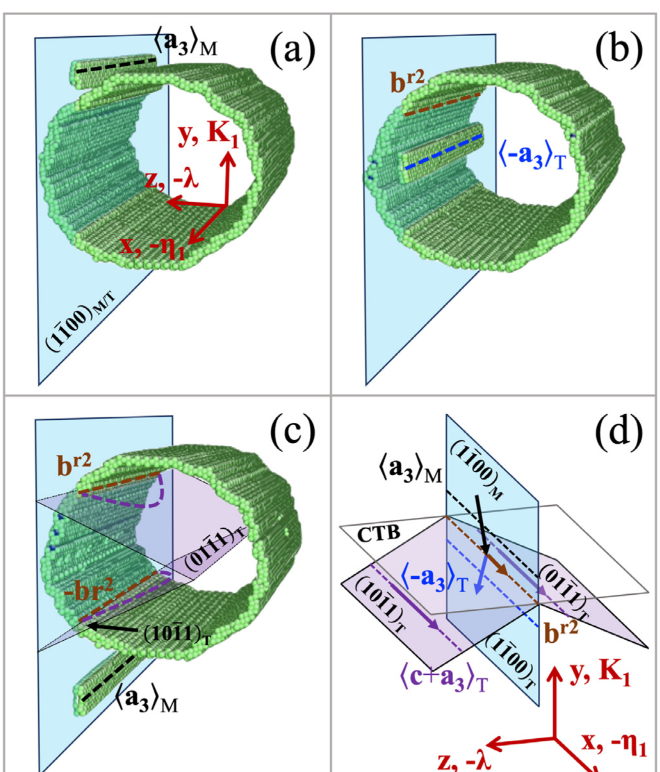

Fig. 8. (a) Initial configuration containing an $\langle \mathbf{a_3}\rangle_M$ dislocation on $(1\bar{1}00)_M$ plane and a $(11\bar{2}2)$ twin. (b) The $\langle \mathbf{a_3}\rangle_M$ dislocation transmits into twin as one $\langle$-$\mathbf{a_3}\rangle_T$ dislocation that glides on $(1\bar{1}00)_T$ plane, leaving a residual dislocation $\mathbf{b^{r2}}$. (c) The $\langle$-$\mathbf{a_3}\rangle_T$ dislocation transmits back to matrix as an $\langle \mathbf{a_3}\rangle_M$ dislocation on $(1\bar{1}00)_M$ plane, leaving a residual dislocation -$\mathbf{b^{r2}}$. (d) Schematics showing planes with co-zone along x-direction.

4.3. Type 3 interactions: $\langle \pm \mathbf{a_1}\rangle_M (0002)_M \rightarrow \langle \mp \mathbf{a_1}\rangle_T \left(01\bar{1}0\right)_T$

Type 3 interactions may result in slip transmission, secondary twinning and local twinning/detwinning, as shown in Fig. 4(a)-**(d)**. Secondary twinning is ruled out when one $\langle \mathbf{a_1}\rangle_M$ dislocation gliding on $(0002)_M$ plane interacts the twin. Slip transmission, $\langle \pm \mathbf{a_1}\rangle_M(0002)_M \rightarrow \langle \mp \mathbf{a_1}\rangle_T(0002)_T$ and $\langle \pm \mathbf{a_1}\rangle_M(0002)_M \rightarrow \langle \mp \mathbf{a_1}\rangle_T \left(01\bar{1}0\right)_T$, may take place on CTB and T-Py_2Py_2 respectively. $(\bar{1}012)$ secondary twinning and $(\bar{2}111)$ secondary twinning may occur on T-Py_1Py_1 interfaces, but $(\bar{1}012)$ secondary twinning is preferred because of the larger λ_m and the most negative ΔE. In the MD simulation we apply loading to promote slip transmission $\langle -\mathbf{a_1}\rangle_M(0002)_M \rightarrow \langle \mathbf{a_1}\rangle_T\left(01\bar{1}0\right)_T$ and $(\bar{1}012)$ secondary twinning.

One incoming $\langle$-$\mathbf{a_1}\rangle_M$ dislocation is introduced in the model, consisting of a mixed partial dislocation and a screw partial dislocation. We apply a stress tensor $\boldsymbol{\sigma_3}$,

$$\boldsymbol{\sigma}_3 = \begin{pmatrix} 0.50 & 0 & 0.46 \\ 0 & -0.20 & 0.29 \\ 0.46 & 0.29 & 0 \end{pmatrix} \text{ GPa} \tag{9}$$

that produces 0.63 GPa RSS on the incoming $\langle \mathbf{a_1}\rangle_M$ dislocation on $(0002)_M$ plane, 0.25 GPa RSS on an outgoing $\langle$-$\mathbf{a_1}\rangle_T$ dislocation on $(01\bar{1}0)_T$ plane, 0.35 GPa RSS associated with $(\bar{1}012)$ secondary twinning and zero RSS associated with twinning/detwinning of the primary twin. As shown in **movie 6**, the $\langle$-$\mathbf{a_1}\rangle_M$ dislocation loops around the twin. No other reactions occur. The same result is observed even under a stress tensor $4\boldsymbol{\sigma_3}$.

We then introduce the 2nd incoming $\langle$-$\mathbf{a_1}\rangle_M$ dislocation to increase the local stress, as shown in Fig. 9(a). The interaction process under the stress tensor $\boldsymbol{\sigma_3}$ is shown in **movie 7** in 3D view. The 1st $\langle$-$\mathbf{a_1}\rangle_M$ dislocation loops around the twin. When the 2nd dislocation is looping around the twin, as shown in Fig. 9(b), a $\langle \mathbf{a_1}\rangle_T$ dislocation on $(01\bar{1}0)_T$ plane is nucleated under the applied stress together with the repulsion of the 2nd $\langle$-$\mathbf{a_1}\rangle_M$ dislocation. The reaction is expressed as,

$$\langle -\mathbf{a_1}\rangle_M \rightarrow \langle \mathbf{a_1}\rangle_T + \mathbf{b^{r3}} \tag{10}$$

The transmission takes place on two T-Py_2Py_2 interfaces, which is consistent with the crystallographic analysis. The $\langle \mathbf{a_1}\rangle_T$ dislocations glide on $(01\bar{1}0)_T$ planes, small segments of the $\langle \mathbf{a_1}\rangle_T$ dislocations cross slip onto $(0002)_T$ planes (Fig. 9(c)).

It is noted that $(\bar{1}012)$ secondary twinning does not happen even if it has larger RSS under the applied loading, and dissociation of $\langle$-$\mathbf{a_1}\rangle_M$ dislocations into PTDs is not observed even under another stress tensor that produces 0.50 GPa twin shear stress. For **type 3** interactions with two $\langle \mathbf{a_1}\rangle_M$ dislocations, we observed similar results as under stress tensor -$\boldsymbol{\sigma_3}$, i.e., $\langle \mathbf{a_1}\rangle_M \rightarrow \langle -\mathbf{a_1}\rangle_T - \mathbf{b^{r3}}$.

4.4. *Type 4 interactions:* $\langle \pm \mathbf{a_1}\rangle_M\left(01\bar{1}0\right)_M \rightarrow \langle \mp \mathbf{a_1}\rangle_T(0002)_T$

Fig. 4(f)-(h) shows possible reactions, slip transmission, secondary twinning and local twinning/detwinning that happen on CTB, T-Py_1Py_1' and T-Py_2Py_2 interfaces when $\langle$-$\mathbf{a_1}\rangle_M$ dislocations on $(01\bar{1}0)_M$ plane interact with the twin. Slip transmission, $\langle \pm \mathbf{a_1}\rangle_M\left(01\bar{1}0\right)_M \rightarrow \langle \mp \mathbf{a_1}\rangle_T(0002)_T$ and $\langle \pm \mathbf{a_1}\rangle_M\left(01\bar{1}0\right)_M \rightarrow \langle \pm \mathbf{a_2}\rangle_T\left(\bar{1}010\right)_T$, may take place on T-$Py_2Py_2$ and CTB respectively, with the former being

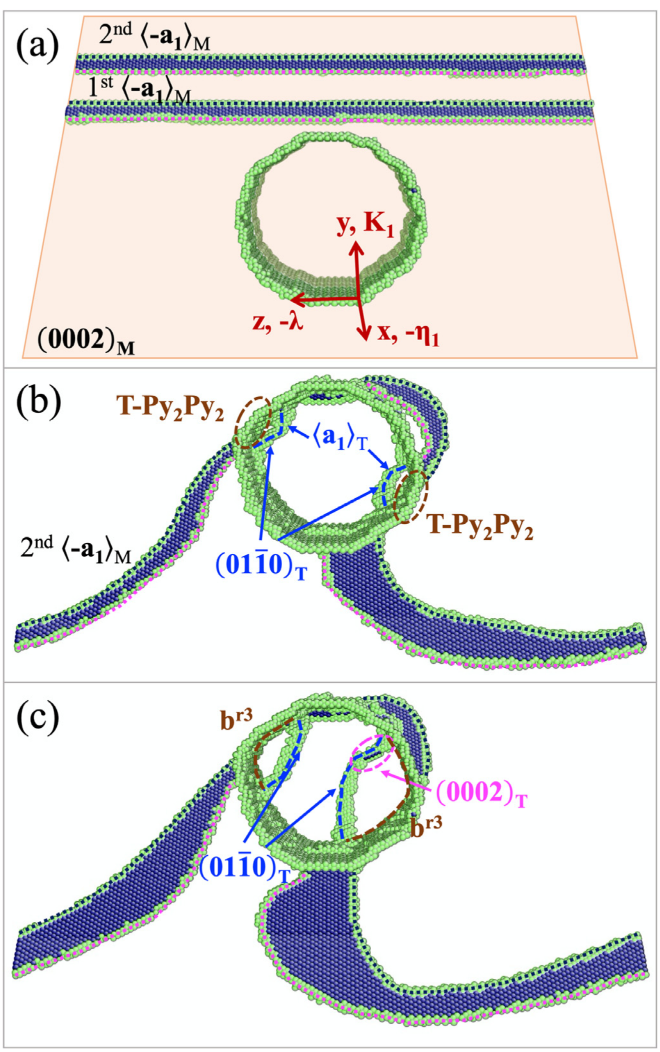

Fig. 9. a) Initial configuration containing two $\langle$-$\mathbf{a_1}\rangle_M$ dislocations on $(0002)_M$ plane and a $(11\bar{2}2)$ twin. (b) After the 1st $\langle$-$\mathbf{a_1}\rangle_M$ dislocation loops the twin, slip transmission $\langle -\mathbf{a_1}\rangle_M(0002)_M \rightarrow \langle \mathbf{a_1}\rangle_T\left(01\bar{1}0\right)_T$ takes place on T-Py_2Py_2 interfaces. (c) The $\langle \mathbf{a_1}\rangle_T$ dislocation locally crosses slip onto $(0002)_T$ plane.

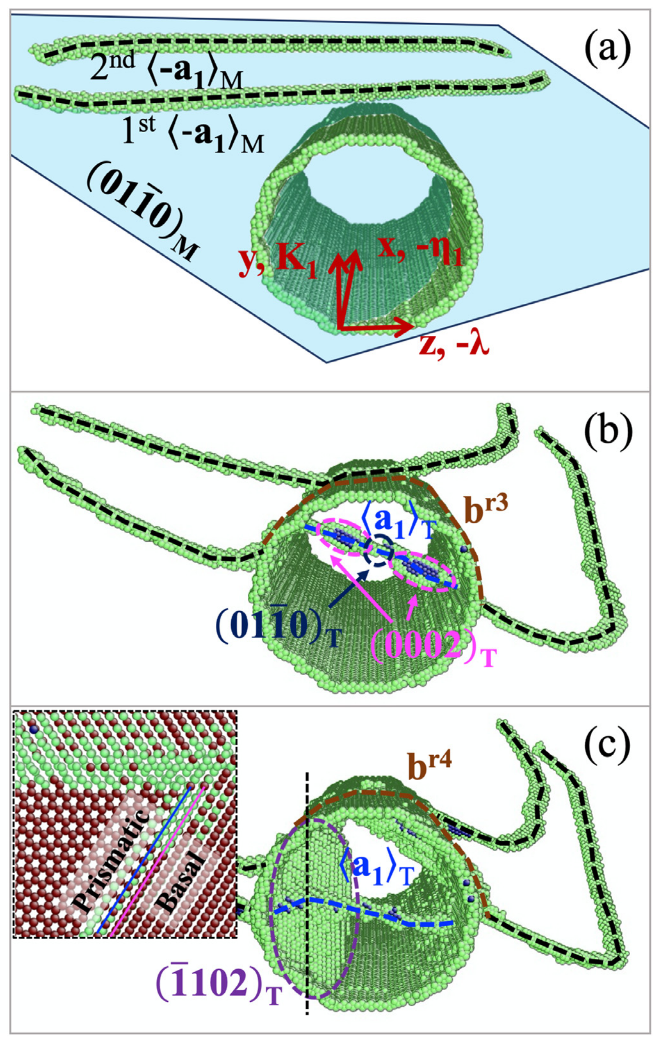

Fig. 10. (a) Initial configuration containing two $\langle$-$\mathbf{a_1}\rangle_M$ dislocations on $(01\bar{1}0)_M$ plane and a $(11\bar{2}2)$ twin. (b) The 1st $\langle$-$\mathbf{a_1}\rangle_M$ dislocation transmits into twin as $\langle \mathbf{a_1}\rangle_T$ dislocation. Major part of the $\langle \mathbf{a_1}\rangle_T$ dislocation glides on $(0002)_T$ planes while minor part cross-slips onto and glides on $(01\bar{1}0)_T$ planes. (c) $(\bar{1}102)$ secondary twinning is activated after slip transmission under stress tensor $\boldsymbol{\sigma_4}'$. The left figure shows the cross-section view normal to λ direction of the $(\bar{1}102)$ secondary twin.

preferred. Secondary twinning can be activated when $\langle\text{-}\mathbf{a_1}\rangle_M$ dislocations are involved. $(\bar{1}102)$ secondary twinning should be predominant over $(\bar{2}111)$ secondary twinning, because $(\bar{1}102)$ secondary twinning has the largest λ_m and the most negative ΔE. But secondary twinning is excluded when $\langle\mathbf{a_1}\rangle_M$ dislocations on $(01\bar{1}0)_M$ plane interact with the twin. In what follows, we apply loading to promote $\langle\mathbf{a_1}\rangle_T$ dislocations on $(0002)_T$ planes and $(\bar{1}102)$ secondary twinning as $\langle\text{-}\mathbf{a_1}\rangle_M$ dislocations approach a $(11\bar{2}2)$ twin.

For one incoming $\langle\text{-}\mathbf{a_1}\rangle_M$ dislocation on a $(01\bar{1}0)_M$ plane as shown in Fig. 10(a), two stress tensors σ_4 and σ_4' are applied to the model respectively. In order to promote slip transmission, the stress tensor σ_4

$$\boldsymbol{\sigma_4} = \begin{pmatrix} 0 & -1.00 & 0.72 \\ -1.00 & 0.93 & -1.15 \\ 0.72 & -1.15 & 0 \end{pmatrix} \text{GPa} \tag{11}$$

is applied, that produces 1.48 GPa RSS on an outgoing $\langle\mathbf{a_1}\rangle_T$ dislocation on $(0002)_T$ plane, 0.69 GPa RSS associated with $(\bar{1}102)$ secondary twinning, and 1.00 GPa RSS associated with twinning/detwinning of the primary twin. In order to maximize the possibility of secondary twinning, another stress tensor $\boldsymbol{\sigma_4}'$

$$\boldsymbol{\sigma_4}' = \begin{pmatrix} 0 & 0 & 0 \\ 0 & 0 & 0 \\ 0 & 0 & -2.00 \end{pmatrix} \text{GPa} \tag{12}$$

is also applied, that produces 1.00 GPa RSS associated with $(\bar{1}102)$ secondary twinning, and zero RSS associated with twinning/detwinning of the primary twin. However, MD simulations show that the $\langle\text{-}\mathbf{a_1}\rangle_M$ dislocation is blocked by the twin and partially loops the $(11\bar{2}2)$ twin under the two stress tensors $\boldsymbol{\sigma_4}$ or $\boldsymbol{\sigma_4}'$. No other reactions take place even if we increase the stress up to $3\boldsymbol{\sigma_4}$ or $2\boldsymbol{\sigma_4}'$.

A 2nd incoming $\langle\text{-}\mathbf{a_1}\rangle_M$ dislocation is introduced to increase the local stress, as shown in Fig. 10(a), under stress tensor $\boldsymbol{\sigma_4}$ that favors slip transmission. The interaction process is shown in **movie 8**. Under the applied stress and the repulsion of the 2nd $\langle\text{-}\mathbf{a_1}\rangle_M$ dislocation, slip transmission $\langle-\mathbf{a_1}\rangle_M \rightarrow \langle\mathbf{a_1}\rangle_T + \mathbf{b^{r3}}$ takes place on a T-Py_2Py_2 interface. As shown in Fig. 10(b), the $\langle\mathbf{a_1}\rangle_T$ dislocation glides on $(0002)_T$ plane while small segments of the $\langle\mathbf{a_1}\rangle_T$ dislocation cross slip onto $(01\bar{1}0)_T$ planes (Fig. 10(b)).

Under stress tensor $\boldsymbol{\sigma_4}$, $(\bar{1}102)$ secondary twinning with $\lambda_m = 0.95$ and $\Delta E = -6.15$ does not happen. **Movie 9** shows the interaction process under stress tensor σ_4' which favors $(\bar{1}102)$ secondary twinning while inhibits slip transmission. As shown in Fig. 10(c), formation of a $(\bar{1}102)$ secondary twin occurs right after slip transmission. The inset on the left of Fig. 10(c) shows a cross-section view normal to $\boldsymbol{\lambda}$ direction of the secondary twin domain. The prismatic plane in the secondary twin is parallel to the basal plane in the primary twin. The 90° misorientation corresponds to the formation of a twin nucleus associated with $\{\bar{1}012\}$ twinning [98, 99].

As for the **type 4** interactions described above, with two $\langle\mathbf{a_1}\rangle_M$ dislocations we observed slip transmission $\langle\mathbf{a_1}\rangle_M \rightarrow \langle-\mathbf{a_1}\rangle_T - \mathbf{b^{r3}}$ and absence of $(\bar{1}102)$ secondary twinning under stress tensors -$\boldsymbol{\sigma_4}$ and -$\boldsymbol{\sigma_4}'$. Primary twinning/detwinning via dissociation of $\langle\pm\mathbf{a_1}\rangle_M$ dislocations into PTDs does not occur under $\pm\boldsymbol{\sigma_4}$, although it induces 1.00 GPa RSS twin shear stress.

5. Conclusions

$\langle\mathbf{a}\rangle$ dislocations on basal or prismatic planes and $\{11\bar{2}2\}$ twins are commonly activated during plastic deformation of Titanium (Ti). We conduct a systematic study of their interactions by both crystallographic analysis and atomistic simulations.

First, we predict possible twin facets associated with a three-dimensional $\{11\bar{2}2\}$ twin corresponding to low index interface according to its crystallography. Next, we determine the low energy interfaces, namely, the normal-TB CTB and three lateral-TBs T-Pr_1Pr_1, T-Py_1Py_1/T-Py_1Py_1' and T-Py_2Py_2/T-Py_2Py_2' with interface energy of 285 mJ/m^2, 400 mJ/m^2, 377 mJ/m^2 and 265 mJ/m^2, respectively. Using 3D MD simulations of the twin, and allowing for relaxation, we observed the formation of these twin boundaries (Fig. 2(b)).

Using crystallographic analysis, we classify the interactions into four types with respect to the character of incoming dislocations, outgoing dislocations/TDs and the interaction TB. **Type 1** is associated with basal $\langle\mathbf{a_3}\rangle$ dislocations that have edge character on CTB, screw character on T-Pr_1Pr_1, and mixed character on the other lateral-TBs. **Type 2** is associated with prismatic $\langle\mathbf{a_3}\rangle$ dislocations that always have mixed character on all TBs. **Type 3** is related to basal $\langle\mathbf{a_1}\rangle$ and $\langle\mathbf{a_2}\rangle$ dislocations that have mirror symmetry about $(1\bar{1}00)$ plane (normal to $\boldsymbol{\lambda}$). **Type 4** is associated with prismatic $\langle\mathbf{a_1}\rangle$ and $\langle\mathbf{a_2}\rangle$ dislocations that share mirror symmetry about $(1\bar{1}00)$ plane (normal to $\boldsymbol{\lambda}$).

Possible reactions are analyzed using Werner's GM [85] and Frank's criteria [86]. Dislocations with opposite signs are considered since they can be activated during reversed loading. Some of the resulting deformation during dislocation-twin interactions, such as twinning/detwinning of primary twin and secondary twinning, are directional and depend on the sign of $\langle\mathbf{a}\rangle$ dislocations. The interaction sites considered are the characteristic TBs, including CTB, T-Pr_1Pr_1, T-Py_1Py_1, T-Py_1Py_1', T-Py_2Py_2 and T-Py_2Py_2' interfaces. Reaction induced slip/twin considered in this analysis include basal $\langle\mathbf{a}\rangle$ slip, prismatic $\langle\mathbf{a}\rangle$ slip, 1st-order pyramidal $\langle\mathbf{a}\rangle$ and $\langle\mathbf{c}+\mathbf{a}\rangle$ slips, and 2nd-order pyramidal $\langle\mathbf{c}+\mathbf{a}\rangle$ slip in twin, as well as twinning/detwinning of primary $(11\bar{2}2)$ twinning on CTBs and secondary $\{\bar{1}012\}$ or $\{11\bar{2}1\}$ tension twinning via nucleation and glide of TDs. According to Werner's GM and Frank's criteria, secondary twinning would be the most likely reaction because it has the largest λ_m and the most negative ΔE. However, these criteria are to be taken as a guidance, since the likelihood of a reaction also depends on other factors, such as dislocation core energy, formation energy of twins, kinetics associated with dislocations and twins, and stresses. In order to account for those factors, and confirm or reject these predictions, we performed 3D atomistic simulations. The applied load is preselected according to crystallographic analysis in order to facilitate a certain deformation mode.

MD simulations demonstrate that secondary twinning in **type 1** interactions and slip transmission in **type 2**–**4** interactions are dominant, and reveal the possibility of forming $\langle\mathbf{c}\rangle$ and $\langle\mathbf{c}+\mathbf{a}\rangle$ dislocations in twins. Moreover, some of these likely reactions take place on lateral TBs other than CTBs. These results extend our understanding of slip transmission, secondary twinning, cross-slip of $\langle\mathbf{a}\rangle$ dislocations and role of characteristic TBs during the interactions.

For **type 1** interactions with $\langle\text{-}\mathbf{a_3}\rangle_M$ dislocations, we only observed dislocation looping around the pre-existing twin. For **type 1** interactions with $\langle\mathbf{a_3}\rangle_M$ dislocations, we observed $(\bar{1}\bar{1}21)$ secondary twinning, only one of three possible reactions predicted by crystallographic analysis. $\langle\mathbf{c}-\mathbf{a_3}\rangle_T$ dislocations on $(\bar{1}\bar{1}22)_T$ planes cannot be directly nucleated because of the large increase of line energy involved. However, the nucleation of $\frac{1}{2}\langle\mathbf{c}-\mathbf{a_3}\rangle_T$ partial dislocations and $\langle\mathbf{c}-\mathbf{a_3}\rangle_T$ full dislocations could be facilitated by $(\bar{1}\bar{1}21)$ secondary twinning: $\frac{1}{2}\langle\mathbf{c}-\mathbf{a_3}\rangle_T$ and $\langle\mathbf{c}-\mathbf{a_3}\rangle_T$ dislocation glide, together with $(\bar{1}\bar{1}21)$ secondary detwinning, reduces the area of secondary TBs. Moreover, this operation may reduce deformation incompatibility between matrix and primary twin. In experiments, the $\{11\bar{2}2\} \rightarrow \{11\bar{2}1\}$ co-family double twins are often observed [28, 84]. Xu et al. [28] proposed the nucleation of $\{11\bar{2}1\}$ secondary twin through the interactions between basal $\langle\mathbf{a}\rangle$ dislocations and $\{11\bar{2}2\}$ CTB. This proposal is confirmed by our simulation results of **type 1** interactions. Meanwhile, the nucleation of $\frac{1}{2}\langle\mathbf{c}-\mathbf{a_3}\rangle_T$ and $\langle\mathbf{c}-\mathbf{a_3}\rangle_T$ dislocations during $\{11\bar{2}1\}$ secondary detwinning can explain the observation of **c**-type dislocations in the vicinity of TBs in TEM [74, 81-83].

For **type 2** interactions, atomistic simulations do not predict the $(2\bar{1}\bar{1}1)$ or $(\bar{1}2\bar{1}1)$ secondary twinning although the reaction has the largest λ_m and the most negative ΔE. This is ascribed to the underestimation of energy change associated with secondary twinning in crystallographic analysis, because nucleation and propagation of secondary twins will change the structure of TBs. Instead, slip transmission of $\langle \mathbf{a_3} \rangle_M$ dislocations into $\langle \mathbf{a_3} \rangle_T$ dislocations on $(1\bar{1}00)_T$ planes in the twin takes place, and can be attributed mainly to the continuity of slip across the boundary. In addition, slip transmission $\langle \mathbf{a_3} \rangle_M \left(1\bar{1}00\right)_M \rightarrow \langle -\mathbf{a_3} \rangle_T \left(1\bar{1}00\right)_T$ does not significantly change the TB because of the screw type of residual dislocations generated, and because the core energy of $\langle \mathbf{a} \rangle$ dislocations is small in Ti [100]. Moreover, residual dislocations $\mathbf{b^{r2}}$ accumulated at TBs may act as sources for the formation of $\langle \mathbf{c}+\mathbf{a_3} \rangle_T$ dislocations on $(10\bar{1}1)_T$ and $(01\bar{1}1)_T$ planes. $\langle \mathbf{c}+\mathbf{a} \rangle$ dislocations have low mobility [9-12] and may dissociate into a glissile $\langle \mathbf{a} \rangle$ dislocation and a sessile $\langle \mathbf{c} \rangle$ dislocation [101, 102]. The **type 2** interactions can be another source for the formation of **c**-type dislocations in the vicinity of TBs [74, 81-83].

For **type 3** interactions, atomistic simulations reproduce the slip transmission $\langle \pm \mathbf{a_1} \rangle_M (0002)_M \rightarrow \langle \mp \mathbf{a_1} \rangle_T \left(01\bar{1}0\right)_T$. This reaction takes place on T-Py_2Py_2 interfaces. Such reactions and their preferred interaction positions are consistent with the prediction by crystallographic analysis. $(\bar{1}012)$ secondary twinning is also likely according to crystallographic analysis, but is not observed in MD simulations. This is because of the underestimation of the energy change in crystallographic analysis. In experiments, $\langle \mathbf{a} \rangle$ dislocations can easily be activated and characterized [74, 81-83] in both twin and matrix. The slip transmission $\langle \pm \mathbf{a_1} \rangle_M (0002)_M \rightarrow \langle \mp \mathbf{a_1} \rangle_T \left(01\bar{1}0\right)_T$ during **type 3** interactions can hardly be confirmed by experimental observation because it is difficult to tell whether the $\langle \mathbf{a} \rangle$ dislocations in twin is produced by the **type 3** interactions.

For **type 4** interactions, atomistic simulations reproduce both slip transmission $\langle \pm \mathbf{a_1} \rangle_M \left(01\bar{1}0\right)_M \rightarrow \langle \mp \mathbf{a_1} \rangle_T (0002)_T$ and $(\bar{1}102)$ secondary twinning. $(\bar{1}102)$ secondary twinning is likely to take place according to crystallographic analysis since it has a λ_m~1 and the most negative ΔE. However, in MD simulations, it takes place under some specific loading and is accompanied by slip transmission. Once again, this is because of the underestimation of the energy change in crystallographic analysis. The $\{11\bar{2}2\} \rightarrow \{10\bar{1}2\}$ non-family double twins are also reported in experiments but are less frequent than $\{11\bar{2}2\} \rightarrow \{11\bar{2}1\}$ double twins [28]. Our simulation results are consistent with the proposal [28] that the nucleation of $\{10\bar{1}2\}$ secondary twin is triggered by the interactions between prismatic $\langle \mathbf{a} \rangle$ dislocations and $\{11\bar{2}2\}$ CTB. In addition, as revealed by the simulations, the nucleation of $\{10\bar{1}2\}$ secondary twins requires specific and large loading in **type 4** interactions while the nucleation of $\{11\bar{2}1\}$ secondary twins takes place easily during **type 1** interactions. This may explain the lower frequency of the observation of $\{11\bar{2}2\} \rightarrow \{10\bar{1}2\}$ double twins.

The simulation results indicate an overall stronger obstruction to $\langle \mathbf{a} \rangle$ dislocations of $\{11\bar{2}2\}$ twins in Ti than that of $\{10\bar{1}2\}$ twins in Mg [52-58, 76, 77]. In Ti, simple obstruction to dislocations or dislocation looping over $\{11\bar{2}2\}$ twins take place when the applied stress is relatively small for **type 2–4** interactions. To trigger reactions such as slip transmission and secondary twinning during **type 2–4** interactions, relatively large loadings (more than 1 GPa) are required. Meanwhile, $\{10\bar{1}2\}$ twins show less obstruction to incoming $\langle \mathbf{a} \rangle$ dislocations. As shown by previous works [52-58, 76, 77], local twinning/detwinning via dissociation of mixed $\langle \mathbf{a} \rangle$ dislocations into PTDs happens simultaneously when the incoming dislocations reach $\{10\bar{1}2\}$ CTB while transmission of mixed/screw $\langle \mathbf{a} \rangle$ dislocations into $\{10\bar{1}2\}$ twin occur even when the applied loadings are relatively small. Consequently, Ti and Mg show different hardening behaviors under loading. For example, compression along extrusion direction on Mg results in a S-shaped stress-strain curve [103]. At the beginning of loading when $\{10\bar{1}2\}$ twins, $\langle \mathbf{a} \rangle$ dislocations and the consequent dislocation-twin interactions are activated [103], the hardening rate is small. At the beginning of compression along normal direction on Ti when $\{11\bar{2}2\}$ twins, $\langle \mathbf{a} \rangle$ dislocations and the consequent dislocation-twin interactions are activated, the hardening rate is larger [104].

The work described above predicts the formation of dislocation structures and secondary twins inside twins and at twin interfaces, following dislocation-twin interaction and slip transmission into the twin. According to the Correspondence Matrix Rule (CMR), understood as the crystallographic transformation of the dislocation line and Burgers vector taking place as a consequence of the twin reorientation, there is no slip system in the $\{11\bar{2}2\}$ twin corresponding to basal $\langle \mathbf{a} \rangle$ slip or prismatic $\langle \mathbf{a} \rangle$ slip in matrix, implying that slip transmission is difficult. However, this is inconsistent with experimental observations. We find that this discrepancy between CMR analysis and experiments originates in ignoring the character of the interaction boundary and secondary twinning. We demonstrate our hypothesis by using Werner's GM [85] and Frank's criteria [86], and 3D MD simulations. A highlight of this work is that 3D atomistic simulation complements the geometric/crystallographic analysis by accounting for the role played by core on reactions, and so provides a comprehensive understanding of dislocation-twin interactions. Different and complex reactions could take place depending on the number and character of incoming dislocations, local atomic structure of the interface, temperature, and local stress field. An overall conclusion of this work is that atomistic simulations, guided and supported by TEM characterization, need to be used for inferring these processes.

Declaration of Competing Interest

The authors declare no competing interests.

Acknowledgments

MG, SX and JW acknowledge the support by the U.S. National Science Foundation (NSF) (CMMI-1661686). L Capolungo and CN Tomé acknowledge the support by the U.S. Dept. of Energy, Office of Science, Basic Energy Sciences (BES) Project FWP 06SCPE401MG. Atomistic simulations were completed utilizing the Holland Computing Center of the University of Nebraska, which receives support from the Nebraska Research Initiative.

Supplementary materials

Supplementary material associated with this article can be found in the online version at doi:10.1016/j.actamat.2020.05.046.

References

[1] A. Astarita, C. Testani, F. Scherillo, A. Squillace, L. Carrino, Beta forging of a Ti6Al4V Component for aeronautic applications: microstructure evolution, Metallogr. Microstruct. Anal.3(6) (2014) 460–467.
[2] F. Froes, Titanium: Physical Metallurgy, Processing, and Applications, ASM International, 2015.
[3] C. Leyens, M. Peters, Titanium and Titanium Alloys: Fundamentals and Applications, John Wiley & Sons, 2003.
[4] R.A. Lebensohn, C.N. Tomé, A self-consistent anisotropic approach for the simulation of plastic deformation and texture development of polycrystals: application to zirconium alloys, Acta Metall. Mater. 41 (9) (1993) 2611–2624.
[5] A.A. Salem, S.R. Kalidindi, S.L. Semiatin, Strain hardening due to deformation twinning in a-titanium: constitutive relations and crystal-plasticity modeling, Acta Mater. 53 (12) (2005) 3495–3502.
[6] H. El Kadiri, A.L. Oppedal, A crystal plasticity theory for latent hardening by glide twinning through dislocation transmutation and twin accommodation effects, J. Mech. Phys. Solids 58 (4) (2010) 613–624.
[7] A.L. Oppedal, H. El Kadiri, C.N. Tomé, G.C. Kaschner, S.C. Vogel, J.C. Baird, M.F. Horstemeyer, Effect of dislocation transmutation on modeling hardening mechanisms by twinning in magnesium, Int. J. Plast. 30-31 (2012) 41–61.
[8] C.N. Tomé, I.J. Beyerlein, R.J. McCabe, J. Wang, Multiscale statistical study of twinning in HCP metals, Integrated Computational Materials Engineering (ICME) for Metals: Concepts and Case Studies, 2018, p. 283.
[9] L. Wang, Z. Zheng, H. Phukan, P. Kenesei, J.S. Park, J. Lind, R.M. Suter, T.R. Bieler, Direct measurement of critical resolved shear stress of prismatic and basal slip

in polycrystalline Ti using high energy X-ray diffraction microscopy, Acta Mater. 132 (2017) 598–610.
[10] J. Gong, A.J. Wilkinson, Anisotropy in the plastic flow properties of single-crystal α titanium determined from micro-cantilever beams, Acta Mater. 57 (19) (2009) 5693–5705.
[11] B. Barkia, V. Doquet, J.P. Couzinié, I. Guillot, E. Héripré, In situ monitoring of the deformation mechanisms in titanium with different oxygen contents, Mater. Sci. Eng. A 636 (2015) 91–102.
[12] J. Williams, R. Baggerly, N. Paton, Deformation behavior of HCP Ti-Al alloy single crystals, Metall. Mater. Trans. A 33 (3) (2002) 837–850.
[13] T. Bieler, P. Eisenlohr, C. Zhang, H. Phukan, M. Crimp, Grain boundaries and interfaces in slip transfer, Current Opin. Solid State Mater. Sci. 18 (4) (2014) 212–226.
[14] A.A. Salem, S.R. Kalidindi, R.D. Doherty, Strain hardening of titanium: role of deformation twinning, Acta Mater. 51 (14) (2003) 4225–4237.
[15] S. Mullins, B.M. Patchett, Deformation microstructures in titanium sheet metal, Metall. Trans. A 12 (1981) 853–863.
[16] F. Lavrentev, The type of dislocation interaction as the factor determining work hardening, Mater. Sci. Eng. 46 (2) (1980) 191–208.
[17] F. Lavrentev, V. Vladimirova, Contribution of primary and “forest” dislocations to deforming stress in zinc crystals under basal slip, Mater. Sci. Eng. 30 (2) (1977) 141–145.
[18] J. Michel, G. Champier, The contribution of pyramidal forest dislocations to the hardening of zinc single crystals, Philos. Mag. A 43 (5) (1981) 1139–1155.
[19] I.J. Beyerlein, C.N. Tomé, A dislocation-based constitutive law for pure Zr including temperature effects, Int. J. Plast. 24 (5) (2008) 867–895.
[20] S. Queyreau, G. Monnet, B. Devincre, Orowan strengthening and forest hardening superposition examined by dislocation dynamics simulations, Acta Mater. 58 (17) (2010) 5586–5595.
[21] S. Xu, Crystallographic Analysis of Twin Variant Selection and Twin-Twin Junctions in Commercially Pure Titanium, Université de Lorraine, 2017.
[22] S. Xu, M. Gong, C. Schuman, J.-S. Lecomte, X. Xie, J. Wang, Sequential {10-12} twinning stimulated by other twins in titanium, Acta Mater. 132 (2017) 57–68.
[23] S. Xu, M. Gong, X. Xie, Y. Liu, C. Schuman, J.-S. Lecomte, J. Wang, Crystallographic characters of {1122} twin-twin junctions in titanium, Philos. Mag. Lett. (2017) 1–13.
[24] D. Chichili, K. Ramesh, K. Hemker, The high-strain-rate response of alpha-titanium: experiments, deformation mechanisms and modeling, Acta Mater. 46 (3) (1998) 1025–1043.
[25] X. Tan, H. Guo, H. Gu, C. Laird, N. Munroe, Cyclic deformation behavior of high-purity titanium single crystals: part II. Microstructure and mechanism, Metall. Mater. Trans. A 29 (2) (1998) 513–518.
[26] X. Li, J. Li, B. Zhou, M. Yu, M. Sui, Interaction of {112 2} twin variants in hexagonal close-packed titanium, J. Mater. Sci. Technol. 35 (4) (2019) 660–666.
[27] H. Li, X. Xu, Q. Sun, X. Zhang, X. Fang, M. Zhu, Investigation of interfacial feature and interactional behavior of {112 2} twin in deformed titanium, J. Alloys Compd. 788 (2019) 1137–1145.
[28] S. Xu, M. Gong, Y. Jiang, C. Schuman, J.-S. Lecomte, J. Wang, Secondary twin variant selection in four types of double twins in titanium, Acta Mater. 152 (2018) 58–76.
[29] S. Xu, L.S. Toth, C. Schuman, J.-S. Lecomte, M.R. Barnett, Dislocation mediated variant selection for secondary twinning in compression of pure titanium, Acta Mater. 124 (2017) 59–70.
[30] L. Xiao, Twinning behavior in the Ti−5 at.% Al single crystals during cyclic loading along [0 0 0 1], Mater. Sci. Eng. A 394 (1−2) (2005) 168–175.
[31] Y. Zhang, Z.S. Dong, J.T. Wang, J.Q. Liu, N. Gao, T.G. Langdon, An analytical approach and experimental confirmation of dislocation−twin boundary interactions in titanium, J. Mater. Sci. 48 (13) (2013) 4476–4483.
[32] P. Franciosi, A. Zaoui, Multislip in fcc crystals a theoretical approach compared with experimental data, Acta Metall. 30 (8) (1982) 1627–1637.
[33] H. El Kadiri, J. Kapil, A.L. Oppedal, L.G. Hector, S.R. Agnew, M. Cherkaoui, S.C. Vogel, The effect of twin−twin interactions on the nucleation and propagation of twinning in magnesium, Acta Mater. 61 (10) (2013) 3549–3563.
[34] L. Jiang, J.J. Jonas, A.A. Luo, A.K. Sachdev, S. Godet, Influence of {10-12} extension twinning on the flow behavior of AZ31 Mg alloy, Mater. Sci. Eng. A 445 (2007) 302–309.
[35] Q. Yu, Y. Jiang, J. Wang, Cyclic deformation and fatigue damage in single-crystal magnesium under fully reversed strain-controlled tension−compression in the [10-10] direction, Scr. Mater. 96 (2015) 41–44.
[36] G.-D. Sim, G. Kim, S. Lavenstein, M.H. Hamza, H. Fan, J.A. El-Awady, Anomalous hardening in magnesium driven by a size-dependent transition in deformation modes, Acta Mater. 144 (2018) 11–20.
[37] R. Reed-Hill, W. Robertson, Additional modes of deformation twinning in magnesium, Acta Metall. 5 (12) (1957) 717–727.
[38] R. Reed-Hill, W. Robertson, The crystallographic characteristics of fracture in magnesium single crystals, Acta Metall. 5 (12) (1957) 728–737.
[39] Q. Yu, J. Zhang, Y. Jiang, Direct observation of twinning−detwinning−retwinning on magnesium single crystal subjected to strain-controlled cyclic tension−compression in [0 0 0 1] direction, Philos. Mag. Lett. 91 (12) (2011) 757–765.
[40] L. Wang, P. Eisenlohr, Y. Yang, T. Bieler, M. Crimp, Nucleation of paired twins at grain boundaries in titanium, Scr. Mater. 63 (8) (2010) 827–830.
[41] Q. Yu, J. Wang, Y. Jiang, R.J. McCabe, N. Li, C.N. Tomé, Twin−twin interactions in magnesium, Acta Mater. 77 (2014) 28–42.
[42] M. Gong, S. Xu, Y. Jiang, Y. Liu, J. Wang, Structural characteristics of {1012} non-cozone twin-twin interactions in magnesium, Acta Mater. 159 (2018) 65–76.
[43] Q. Yu, J. Wang, Y. Jiang, R.J. McCabe, C.N. Tomé, Co-zone {-1012} twin interaction in magnesium single crystal, Mater. Res. Lett. 2 (2) (2014) 82–88.
[44] Q. Sun, A. Ostapovets, X. Zhang, L. Tan, Q. Liu, Investigation of twin−twin interaction in deformed magnesium alloy, Philos. Mag. 98 (9) (2018) 741–751.
[45] A. Berghezan, A. Fourdeux, S. Amelinckx, Transmission electron microscopy studies of dislocations and stacking faults in a hexagonal metal: zinc, Acta Metall. 9 (5) (1961) 464–490.
[46] G. Proust, C. Tomé, G. Kaschner, Modeling texture, twinning and hardening evolution during deformation of hexagonal materials, Acta Mater. 55 (6) (2007) 2137–2148.
[47] K.D. Molodov, T. Al-Samman, D.A. Molodov, Profuse slip transmission across twin boundaries in magnesium, Acta Mater. 124 (2017) 397–409.
[48] F. Wang, S.R. Agnew, Dislocation transmutation by tension twinning in magnesium alloy AZ31, Int. J. Plast. 81 (2016) 63–86.
[49] S. Morozumi, M. Kikuchi, H. Yoshinaga, Electron Microscope Observation in and around (1-102) Twins in Magnesium, Trans. Jpn. Inst. Metals 17 (3) (1976) 158–164.
[50] D.I. Tomsett, M. Bevis, The incorporation of basal slip dislocations in {1012} twins in zinc crystals, Philos. Mag. 19 (157) (1969) 129–140.
[51] D.I. Tomsett, M. Bevis, The formation of stacking faults in {1012} twins in zinc as a result of slip dislocation-deformation twin interactions, Philos. Mag. 19 (159) (1969) 533–537.
[52] A. Serra, D.J. Bacon, Computer simulation of screw dislocation interactions with twin boundaries in HCP metals, Acta Metall. Mater. 43 (12) (1994) 4465–4481.
[53] M. Gong, G. Liu, J. Wang, L. Capolungo, C.N. Tomé, Atomistic simulations of interaction between basal <a>dislocations and three-dimensional twins in magnesium, Acta Mater. 155 (2018) 187–198.
[54] J. Wang, I.J. Beyerlein, C.N. Tomé, Reactions of lattice dislocations with grain boundaries in Mg: implications on the micro scale from atomic-scale calculations, Int. J. Plast. 56 (2014) 156–172.
[55] A. Serra, D.J. Bacon, R.C. Pond, Dislocations in interfaces in the hcp metals—I. Defects formed by absorption of crystal dislocations, Acta Mater. 47 (5) (1999) 1425–1439.
[56] A. Serra, D.J. Bacon, R.C. Pond, Twins as barriers to basal slip in hexagonal-close-packed metals, Metall. Mater. Trans. A 33 (3) (2002) 809–812.
[57] J. Wang, I.J. Beyerlein, J.P. Hirth, Nucleation of elementary {-1011} and {-1013} twinning dislocations at a twin boundary in hexagonal close-packed crystals, Modell. Simul. Mater. Sci. Eng. 20 (2) (2012) 024001.
[58] H. El Kadiri, C.D. Barrett, J. Wang, C.N. Tomé, Why are {10-12} twins profuse in magnesium? Acta Mater. 85 (2015) 354–361.
[59] I.J. Beyerlein, J. Wang, M.R. Barnett, C.N. Tome, Double twinning mechanisms in magnesium alloys via dissociation of lattice dislocations, Proc. R. Soc. A Math. Phys. Eng. Sci. 468 (2141) (2012) 1496–1520.
[60] L. Capolungo, I.J. Beyerlein, G.C. Kaschner, C.N. Tomé, On the interaction between slip dislocations and twins in HCP Zr, Mater. Sci. Eng. A 513-514 (2009) 42–51.
[61] A.W. Sleeswyk, C.A. Verbraak, Incorporation of slip dislocations in mechanical twins—I, Acta Metall. 9 (10) (1961) 917–927.
[62] M.H. Yoo, Interaction of slip dislocations with twins in hcp metals, Trans. Metall. Soc. AIME 245 (1969) 2061-2060.
[63] I. Saxl, The incorporation of slip dislocations in twins, Czechoslovak J. Phys. 18 (1) (1968) 39–49.
[64] M.H. Yoo, C.T. Wei, Growth of deformation twins in zinc crystals, Philos. Mag. 14 (129) (1966) 573–587.
[65] M. Niewczas, Lattice correspondence during twinning in hexagonal close-packed crystals, Acta Mater. 58 (17) (2010) 5848–5857.
[66] D.M. Vallance, M. Bevis, The interaction of slip dislocations with twin boundaries, Scr Mater. 4 (9) (1970) 681–684.
[67] P.W. Bakarian, C.H. Mathewson, Slip and twinning in Magnesium single crystals at elevated temperatures, Trans. Metall. Soc. AIME 152 (1943) 226–254.
[68] P.B. Price, Nucleation and growth of twins in dislocation-free zinc, Proc. R. Soc. Lond. A Math. Phys. Eng. Sci. 260 (1301) (1961) 251–262.
[69] R.E. Cooper, J. Washburn, Stress-induced movement of twin boundaries in zinc, Acta Metall. 15 (4) (1967) 639–647.
[70] S. Lay, G. Nouet, Interaction of slip dislocations with the (0112) twin interface in zinc, Philos. Mag. A 70 (6) (1994) 1027–1044.
[71] J.I. Dickson, C. Robin, The incorporation of slip dislocations in {1-102} twins in zirconium, Mater. Sci. Eng. 11 (5) (1973) 299–302.
[72] D.G. Westlake, Twinning in Zirconium, Acta Metall. 9 (4) (1961) 327–331.
[73] F.C. Frank, LXXXIII. Crystal dislocations.—Elementary concepts and definitions., The London, Edinburgh, and Dublin Philosophical Magazine and Journal of Science42(331) (1951) 809−819.
[74] D. Bhattacharyya, E.K. Cerreta, R. McCabe, M. Niewczas, G.T. Gray, A. Misra, C.N. Tomé, Origin of dislocations within tensile and compressive twins in pure textured Zr, Acta Mater. 57 (2) (2009) 305–315.
[75] S.G. Song, G.T. Gray, Structural interpretation of the nucleation and growth of deformation twins in Zr and Ti—II. Tem study of twin morphology and defect reactions during twinning, Acta Metall. Mater. 43 (6) (1995) 2339–2350.
[76] A. Serra, D.J. Bacon, A new model for {10-12} twin growth in hcp metals, Philos. Mag. A 73 (2) (1996) 333–343.
[77] J. Wang, L. Liu, C.N. Tomé, S.X. Mao, S.K. Gong, Twinning and de-twinning via glide and climb of twinning dislocations along serrated coherent twin boundaries in hexagonal-close-packed metals, Mater. Res. Lett. 1 (2) (2013) 81–88.
[78] F. Wang, C.D. Barrett, R.J. McCabe, H. El Kadiri, L. Capolungo, S.R. Agnew, Dislocation induced twin growth and formation of basal stacking faults in {101 2} twins in pure Mg, Acta Mater. 165 (2019) 471–485.

[79] M. Yoo, Slip, twinning, and fracture in hexagonal close-packed metals, Metall. Trans. A 12 (3) (1981) 409–418.
[80] B.A. Bilby, A.G. Crocker, The theory of the crystallography of deformation twinning, Phys. Eng. Sci. 288 (1413) (1965) 240–255.
[81] O.-.T. Woo, G. Carpenter, S. MacEwen, < c>-Component dislocations in zirconium alloys, J. Nuclear Mater. 87 (1) (1979) 70–80.
[82] S. Song, G. Gray, Influence of temperature and strain rate on slip and twinning behavior of Zr, Metall. Mater. Trans. A 26 (10) (1995) 2665–2675.
[83] Q. Sun, J. Tu, L. Tan, M. Zhang, X. Fang, M. Zhu, X. Zhang, Transmission electron microscopy study of< c+ a>dislocations within 112 2 twin in deformed titanium, Mater. Charact. 151 (2019) 146–150.
[84] H. Qin, J.J. Jonas, Variant selection during secondary and tertiary twinning in pure titanium, Acta Mater. 75 (2014) 198–211.
[85] E. Werner, W. Prantl, Slip transfer across grain and phase boundaries, Acta Metall. Mater. 38 (3) (1990) 533–537.
[86] J.P. Hirth, J. Lothe, Theory of Dislocations, 2nd ed., Wiley, New York, 1982.
[87] M. Gong, J.P. Hirth, Y. Liu, Y. Shen, J. Wang, Interface structures and twinning mechanisms of twins in hexagonal metals, Mater. Res. Lett. (2017) 1–16.
[88] Y. Liu, N. Li, S. Shao, M. Gong, J. Wang, R.J. McCabe, Y. Jiang, C.N. Tome, Characterizing the boundary lateral to the shear direction of deformation twins in magnesium, Nat. Commun. 7 (2016) 11577.
[89] J.P. Hirth, G. Hirth, J. Wang, Disclinations and disconnections in minerals and metals, Proc. Natl. Acad. Sci. 117 (1) (2020) 196–204.
[90] M. Gong, S. Xu, D. Xie, S. Wang, J. Wang, C. Schuman, J.-.S. Lecomte, Steps and {112 1} secondary twinning associated with {112 2} twin in titanium, Acta Mater. 164 (2019) 776–787.
[91] R.R. Zope, Y. Mishin, Interatomic potentials for atomistic simulations of the Ti-Al system, Phys. Rev. B 68 (2) (2003) 024102.
[92] D.M. Barnett, J. Lothe, An image force theorem for dislocations in anisotropic bicrystals, J. Phys. F: Metal Phys. 4 (10) (1974) 1618.
[93] R.C. Pond, A. Serra, A.P. Sutton, The crystallography and atomic structure of line defects in twin boundaries in hexagonal-close-packed metals, Metall. Mater. Trans. A 22 (6) (1991) 1185–1196.
[94] A. Serra, D.J. Bacon, R.C. Pond, The crystallography and core structure of twinning dislocations in hcp metals, Acta Metall. 36 (12) (1988) 3183–3203.
[95] I. Beyerlein, J. Wang, K. Kang, S. Zheng, N. Mara, Twinnability of bimetal interfaces in nanostructured composites, Mater. Res. Lett. 1 (2) (2013) 89–95.
[96] A. Serra, R.C. Pond, D.J. Bacon, Computer simulation of the structure and mobility of twinning disclocations in HCP metals, Acta Metall. Mater. 39 (7) (1991) 1469–1480.
[97] B. Yin, Z. Wu, W.A. Curtin, Comprehensive first-principles study of stable stacking faults in HCP metals, Acta Mater. 123 (2017) 223–234.
[98] J. Wang, S.K. Yadav, J.P. Hirth, C.N. Tomé, I.J. Beyerlein, Pure-shuffle nucleation of deformation twins in hexagonal-close-packed metals, Mater. Res. Lett. 1 (3) (2013) 126–132.
[99] A. Ostapovets, R. Gröger, Twinning disconnections and basal−prismatic twin boundary in magnesium, Modell. Simul. Mater. Sci. Eng. 22 (2) (2014).
[100] M. Ghazisaeidi, D.R. Trinkle, Core structure of a screw dislocation in Ti from density functional theory and classical potentials, Acta Mater. 60 (3) (2012) 1287–1292.
[101] Z. Wu, W.A. Curtin, Mechanism and energetics of <c + a>dislocation cross-slip in hcp metals, Proc. Natl. Acad. Sci. U.S.A 113 (40) (2016) 11137–11142.
[102] Z. Wu, W.A. Curtin, The origins of high hardening and low ductility in magnesium, Nature 526 (7571) (2015) 62–67.
[103] Q. Ma, H. El Kadiri, A.L. Oppedal, J.C. Baird, B. Li, M.F. Horstemeyer, S.C. Vogel, Twinning effects in a rod-textured AM30 Magnesium alloy, Int. J. Plast. 29 (2012) 60–76.
[104] M. Wronski, M.A. Kumar, L. Capolungo, R.J. McCabe, K. Wierzbanowski, C.N. Tome, Deformation behavior of CP-titanium: experiment and crystal plasticity modeling, Mater. Sci. Eng. A 724 (2018) 289–297.